ANISOTROPIC FLOW FLUCTUATIONS IN VERY CENTRAL PB-PB $\sqrt{S_{NN}}$ = 2.76 TEV COLLISIONS

A Dissertation Presented to

the Faculty of the Department of Physics

University of Houston

In Partial Fulfillment

of the Requirements for the Degree

Doctor of Philosophy

By

Muqing Jin

May 2019

ANISOTROPIC FLOW FLUCTUATIONS IN VERY CENTRAL PB-PB $\sqrt{S_{NN}}$ = 2.76 TEV COLLISIONS

Muqing Jin

APPROVED:

Anthony R. Timmins, Chairman
Dept. of Physics

Andrew Renshaw
Dept. of Physics

Ed V. Hungerford
Dept. of Physics

Donald J. Kouri
Dept. of Physics

Bernhard Rappenglueck
Dept. of Geophysics

Dean, College of Natural Sciences and Mathematics

ANISOTROPIC FLOW FLUCTUATIONS IN VERY CENTRAL PB-PB $\sqrt{S_{NN}}$ = 2.76 TEV COLLISIONS

An Abstract of a Dissertation

Presented to

the Faculty of the Department of Physics

University of Houston

In Partial Fulfillment

of the Requirements for the Degree

Doctor of Philosophy

By

Muqing Jin

May 2019

Abstract

An extremely hot and dense medium where quarks and gluons become deconfined from their typical hadronic states known as the Quark-Gluon Plasma (QGP), is created at the Large Hadron Collider (LHC). The collective flow of the system plays a critical role in establishing the equation of state for QGP. Among the different orders of azimuthal flow, the second order elliptic flow (v_2) has received much attention, and will be analyzed in the ultra-central collision (0-5%) centrality range. Various hydrodynamic simulations show that v_2 correlates almost linearly with the initial eccentricity ε_2 of the system (which fluctuates on an event by event basis). Measurements of v_2 fluctuations are extremely sensitive to the initial state configuration. An unfolding method has been used to obtain the underlying v_2 distributions from Pb-Pb collisions with a center of mass energy per nucleon of 2.76 TeV.

I dedicate my dissertation work to all of my family members. A special feeling of gratitude to my wife, and my loving parents whose never left my side and providing me countless of support and encouragement.

Acknowledgements

Working at the University of Houston as a Ph.D student over the past five years has proved to be a great and fruitful experience. Firstly, I would like to express my sincere gratitude towards my research advisor, Prof. Anthony R. Timmins for giving me the opportunity to work on the cutting edge of fundamental physics at ALICE experiment. His continuous support of my Ph.D study and related research, patience, motivation, and immense knowledge has provided me with excellence guidance throughout my Ph.D program. Without his guidance, it could not be possible for me to complete my Ph.D pursuit. I cannot imagine having a better advisor and mentor for my Ph.D study.

Besides my advisor, I would like to thank Prof. Rene Bellwied. The insightful comments in every group meeting widen my knowledge of particle physics. I also would like to thank Prof. Andrew Renshaw, Prof. Ed V. Hungerford, Prof. Donald J. Kouri and Prof. Bernhard Rappenglueck. The insightful questions and comments encourage me to better understanding the fundamental physics underlying my research.

Also, I would like to thank our formal senior Ph.D student, who have already graduated, Dr. Fabian Ng. He taught me invaluable lessons on coding, the logic behind the codes, and much more.

Last but not the least, I would like to thank my family: my parents, my wife, and to my other relatives in China for supporting me spiritually throughout writing this dissertation and my life in general.

Contents

List of Figures

List of Tables

Chapter 1

Introduction

The standard model (SM), quantum chromodynamics (QCD), the quark-gluon plasma (QGP), and collective flow will be reviewed in this chapter. In Section 1.1, the standard model will be briefly explained, which is a theory that describes fundamental particles and their interactions. Subsequently, the most successful theory of the strong interaction, quantum chromodynamics (QCD) will be introduced. Quarks interact via the strong nuclear force and the strong force is mediated by gluons. In Section 1.3, the quark-gluon plasma (QGP) will be discussed, which is a state of matter that exists when the temperature is higher than its corresponding phase transition temperature. In the quark-gluon plasma (QGP), quarks and gluons are deconfined and the degrees of freedom in this state are color charged. In Section 1.4, collective flow, the collective behavior of the system produced in the heavy ion collisions, will be introduced. It is also one of the most important probes to study the quark-gluon plasma (QGP). In Section 1.5, the chapter will finish with an outline

of this thesis.

1.1 The Standard Model

The Standard Model is currently the best theory that describes elementary particles and the interactions between them. The interactions include the *weak force*, the *strong nuclear force*, and the *electromagnetic force.* A critical property of elementary particles is their spin. As shown in Figure 1.1, the seventeen known elementary particles can be divided into twelve fermions (spin = $\frac{1}{2}$), four gauge bosons (the spin is a nonzero integer), and one Higgs boson (spin = 0). There are three generations of fermions and the mass of each generation is different. Each generation contains two quarks and two leptons. So there are also 6 types of quarks (up, down, charm, strange, top and bottom quarks) and 6 types of leptons (electron, muon, tau, and their corresponding neutrinos).

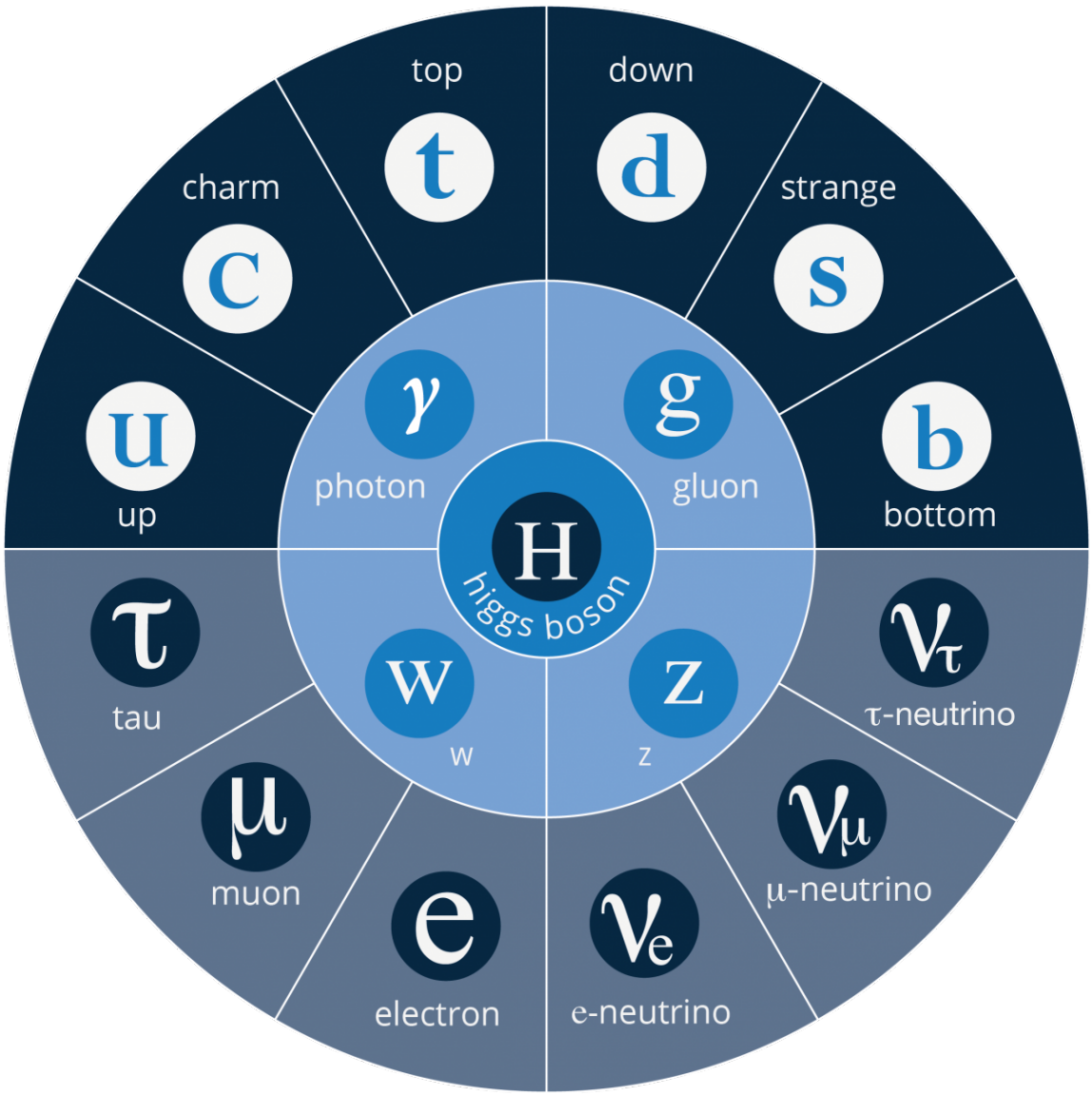

Figure 1.1: Schematic view of the Standard Model [1].

The gauge bosons are the force carriers. The electromagnetic force is mediated by photons, and the weak force is mediated by W and Z bosons. Quarks interact via the strong nuclear force mediated by gluons. Lastly, the recently discovered Higgs

boson is the particle that couples to other elementary particles which have a nonzero mass.

1.2 Quantum Chromodynamics (QCD)

Quantum Chromodynamics (QCD) is a fundamental theory of the strong nuclear interaction. It is the most successful theory that describes the strong interaction between quarks and gluons. The word chromodynamics does not refer to the usual concept of visible color, but is an analogy to electric charge in Quantum Electrodynamics (QED). There are six color charges in QCD: red, blue, green, anti-red, anti-blue, and anti-green. The combination of red, green, blue is color neutral, as is the combination of anti-red, anti-green, anti-blue. The combination of two opposite color charges, such as red and anti-red, is also color neutral. A hadron consists of a bound state of three quarks, known as a *baryon*, or a quark and anti-quark pair, known as a *meson*. Gluons are exchange particles that glue the quarks via the strong potential. QCD predicts that the long distance between quarks (which leads to confinement) and the short distance behavior (asymptotic freedom) are rather distinct.

To understand this better, the strong potential between two quarks can be described as follows:

$$V(r) = -\frac{4}{3}\frac{\alpha_s}{r} + \kappa r, \tag{1.1}$$

where r is the distance between the quarks, and κ is a constant which is analogous

to the constant in the string tension equation. The variable α_s is the strong coupling constant, and depends on the four momentum transfer Q^2 between the interacting quarks. When two quarks are close and r is small, which would be the result of a large momentum transfer, the second term in the strong potential tends to be zero. In addition, α_s also decreases with increasing Q^2, and the net result is for the interaction to become weak, and the interacting quarks resemble free particles. This is known as *asymptotic freedom.* When the distance between the quarks increases, the second term of the strong potential will dominate and increase with distance. As a result, in principle it would require an infinite amount of energy to completely separate them. In practice, the production of a new quark anti-quark pair becomes energetically favorable, and will be formed when the separation distance is more than the diameter of a hadron (roughly 1 fm). This mechanism explains why single quarks are not observed in nature, but are always confined in a color neutral hadron. This is known as *confinement* [21].

The phenomenon of asymptotic freedom leads to the possibility of the formation of a state of matter known as the the *Quark-Gluon Plasma* (QGP) [22]. At large enough energies, the interaction potential between quarks is weak enough to allow them to move over distances larger than the size of a hadron. This is a deconfined state of nuclear matter, where quarks and gluons are the relevant degrees of freedom, as opposed to a hadronic gas.

1.3 Quark-gluon Plasma (QGP)

Figure 1.2 illustrates the nuclear phase diagram, which shows regions the color charged QGP is believed to occur, and other regions where the color neutral hadronic matter exists. The y-axis is the temperature T, and the x-axis is the net baryon number density. Generally speaking, a QGP will be formed when the nuclear matter either has a high temperature, or a high net baryon number density. There is a corresponding phase transition between the QGP and hadronic gas. At high baryon densities, this is believed to be first order, whereas at high temperatures this is believed to be a cross-over transition. The yellow circle indicates a possible critical point [23], which is a specific temperature and baryon density where the first order phase transition would cease. The smooth crossover curve shows the region where there is no distinct phase transition from hadronic matter to the QGP. The low-temperature and high-baryon density region of the phase diagram is believed to be the matter found in the neutron stars. Above a certain high critical temperature, quarks and gluons confined in the hadrons undergoes a phase transition to the deconfined QGP. In the early universe, the state of matter just after the Big Bang is believed to be a high temperature QGP with zero net baryon density.

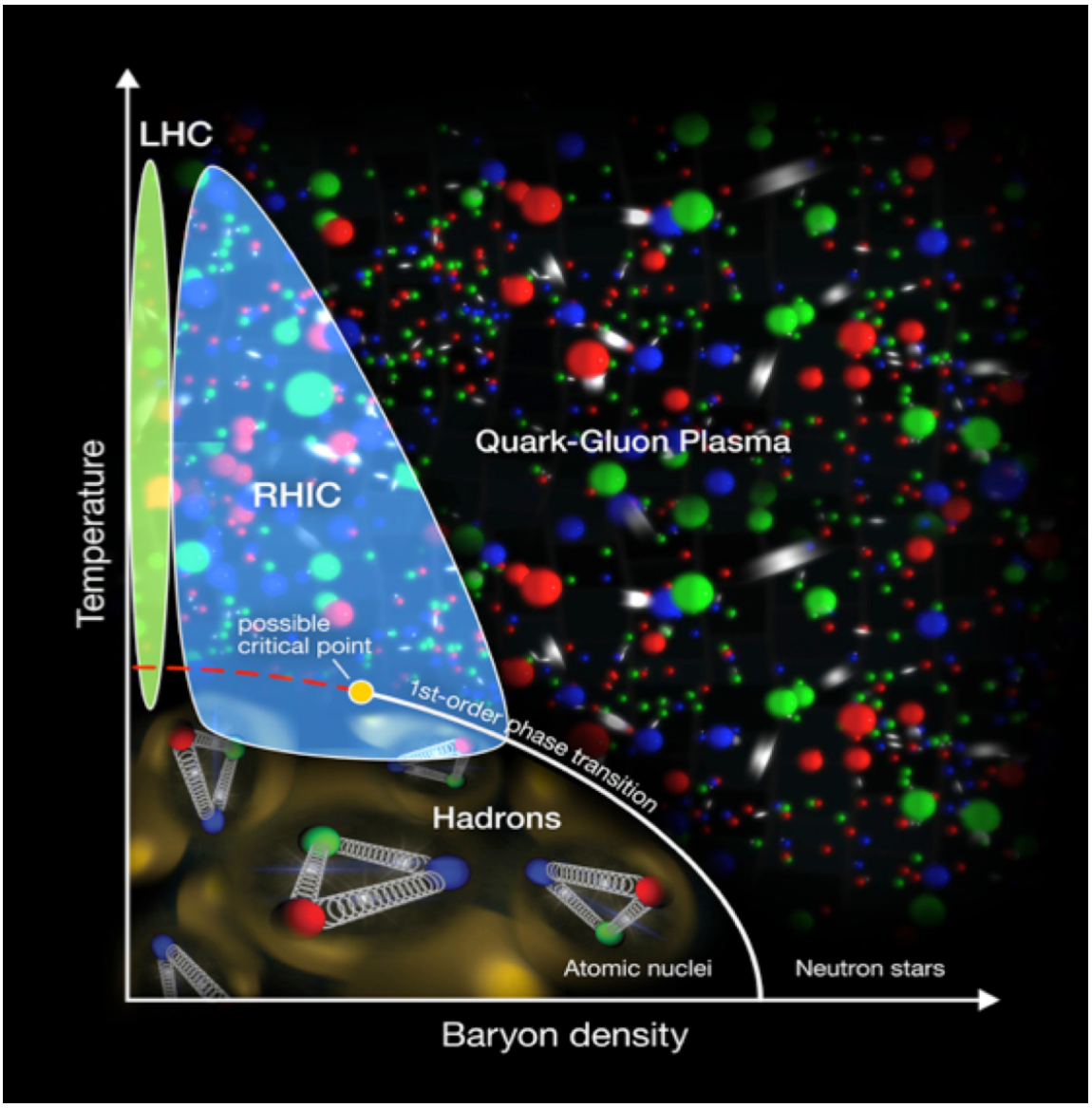

Figure 1.2: QCD phase diagram [2].

According to the big bang theory, the universe started from a single point approximately 13.7 billions years ago. Just after time-zero of the big bang, the quark-gluon plasma formed. It would have been an extremely hot and dense state of matter, with

energy densities exceeding $\sim$1 GeV/fm^3 and temperatures above T $\sim 10^{15}$ K [24]. As the system cooled down, the quarks and gluons become confined into hadrons. With high energy heavy ion collisions, a high temperature QGP is believed formed for a short period of time. To study QGP, two heavy ions are accelerated to a speed very close to the speed of light, and then they collide with each other. A very large amount of energy is deposited in a very short amount of time and in a very small volume. This is believed to be large enough to "melt" the atomic nuclei, and reach the critical temperature needed to produce the QGP. Evidence for QGP formation has been found at the Relativistic Heavy Ion Collider (RHIC) and the Large Hadron Collider (LHC) facilities.

The QGP formed in a heavy-ion collision experiment cannot be directly observed. The matter formed in the collision cools down first, the quarks hadronize, and final state hadrons can be observed in a detector. In the early stages of collision, the temperature of the medium exceeds the critical temperature T_c, which is a temperature when the transition to partonic degrees of freedom occurs, and the medium becomes the QGP. The QGP then continues to expand under very high pressure gradients and eventually cools down. When the temperature drops below T_c, the system begins to form a hadronic gas. As the cooling process progresses and reaches the chemical freeze-out temperature T_{ch}, inelastic scattering ceases and the composition of hadrons is fixed. Finally, the kinetic freeze-out temperature T_{fo} is reached and the kinetic properties of particles no longer change via elastic collisions. Figure 1.3 shows the evolution of the QGP starting from the colliding the heavy-ions to the final state, which is as mentioned is accessible to detectors. Therefore, the behavior of

the QGP can only be inferred from the detected final state particles. The collective expansion of QGP is an important physical observable, which will be discussed in the next section.

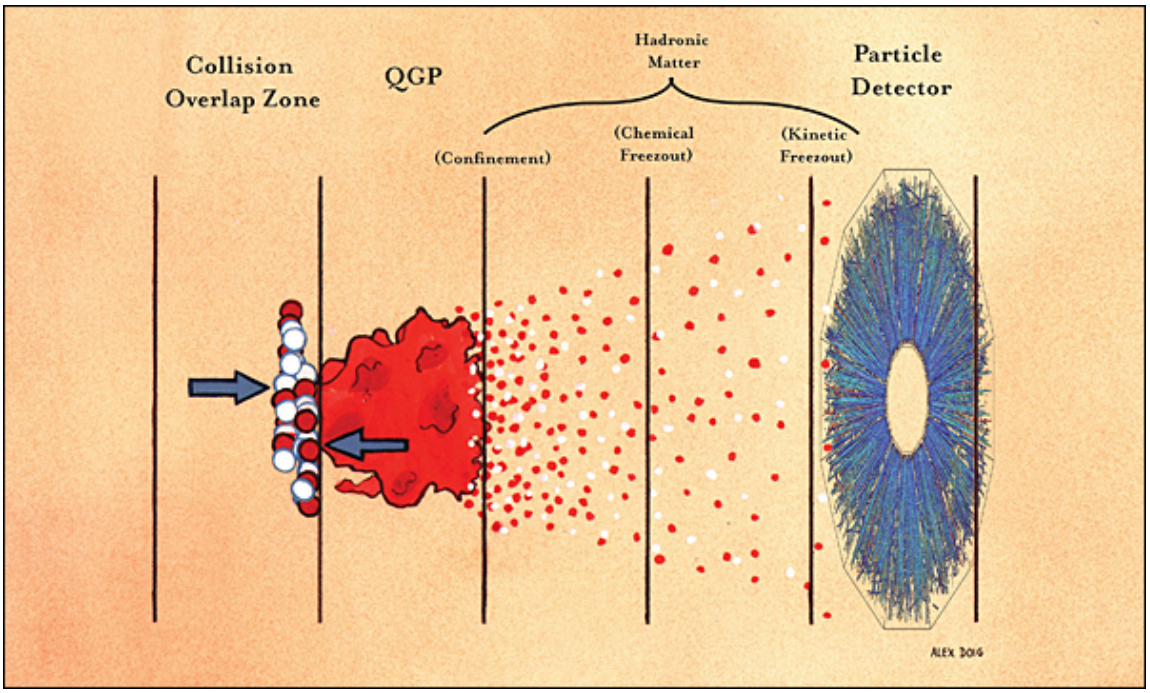

Figure 1.3: Evolution of the production of QGP from colliding the two heavy ions. Only the final particles or their decay products are collected by the detectors [3].

1.4 Collective Expansion

The properties of the formed system in a heavy ion collision can be studied from the azimuthal momentum distribution of the emitted particles. If the system is in thermal equilibrium, the resulting pressure gradients generate a common velocity profile for the outgoing particles, which is known as *collective flow*. The term collective flow

includes a common radial expansion called radial flow, and an anisotropic expansion called anisotropic flow [25]. The most dominant contribution to anisotropic flow is elliptic flow.

Elliptic flow is defined as the second harmonic coefficient of the azimuthal Fourier decomposition of the momentum distribution, and describes the final state azimuthal anisotropy of particles in the plane transverse to the beam direction. Elliptic flow is an important observable which directly reflects the initial spatial anisotropy of the nuclear overlap region. It is especially sensitive to the early stages of system evolution, when the QGP is believed to occur, and measurements of elliptic flow provide access to the equation of state of the QGP.

The process is demonstrated in Figure 1.4. The variable b is the impact parameter, which refers to the length connecting the centers of the colliding nuclei in the transverse plane, and z is the beam direction. The impact parameter direction x and the beam direction z correspond to the reaction plane direction. There are larger pressure gradients in the x direction compared to the y direction, which leads to a greater expansion along the x direction. The coordinate space anisotropy in the initial state is then transferred to a momentum space anisotropy in the final produced particles.

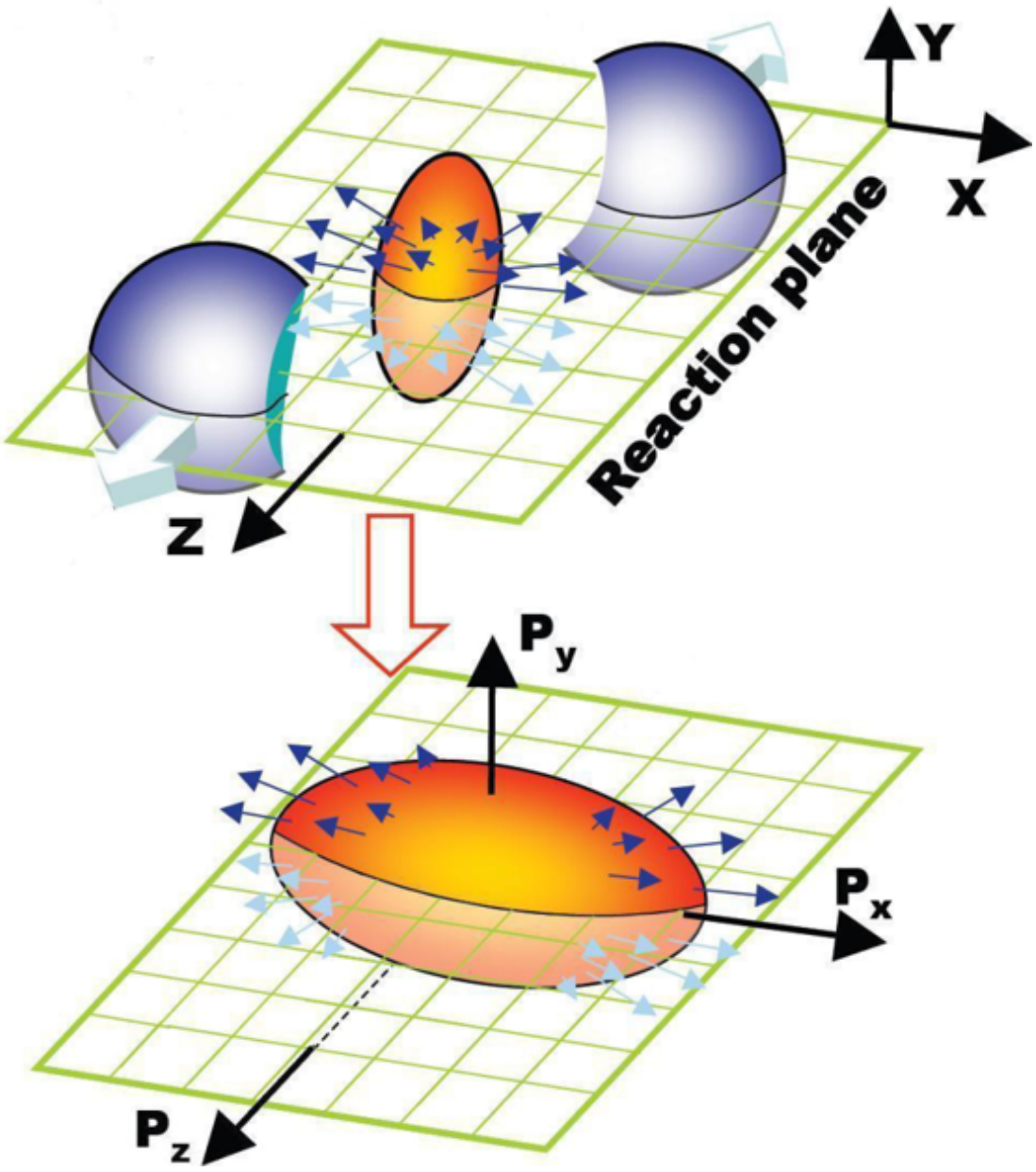

Figure 1.4: Visual illustration of a collision where the overlapping volume forms an almond shape in the reaction plane.

1.5 Dissertation Outline

This chapter has introduced the concepts of elementary particles, the Quantum Chromodynamics, the Quark Gluon Plasma, and the collective expansion of QGP in heavy ion collisions. These concepts are important for understanding the research topic of this thesis: elliptic-flow fluctuations. These flow fluctuations are very sensitive to the initial state. By measuring flow fluctuations, we can obtain further information of the initial state. In particular, since anisotropic flow is the result of an anisotropic initial state and the QGP medium response, measurements that constrain the initial state are crucial for understanding the medium response.

The next chapter describes the high-energy physics lexicon. The experimental setup and the detectors used for this study will be provided in Chapter 3. The methods used to measure anisotropic flow will be discussed in Chapter 4. The analysis details will be provided in Chapter 5. The main results will be shown in Chapter 6 and 7. The thesis concludes with discussion of the results in Chapter 8.

Chapter 2

Definitions and Terminology

To better understand measurements made from heavy ion collisions, some terminologies will be defined and explained in this chapter.

2.1 Azimuthal Angle and Transverse Momentum

Figure 2.1 shows the coordination space used in high energy physics, in the vicinity of the ALICE high-energy physics detector. The center of the detector corresponds to $x = y = z = 0$. The blue plane (xy plane), perpendicular to the beam direction in the z plane, is called the *transverse plane.* The angle between x direction and the projection of the produced particle direction in transverse plane is the referred to as the *azimuthal angle* and is denoted as φ. In Figure 2.1, φ is shown according to negative x direction, therefore a negative sign is provided before φ.

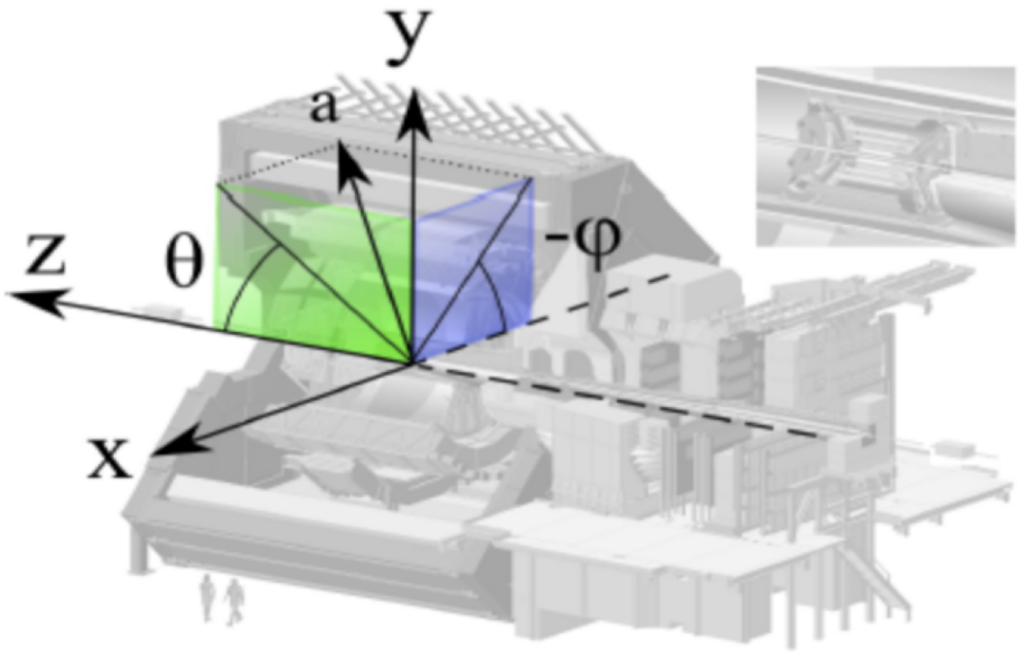

Figure 2.1: Schematic view of the coordinate in the ALICE detector [4].

The momentum vector of a produced particle from a collision in the transverse plane is the *transverse momentum* (p_T). This is an important measurable physical quantity of final state particles because transverse momentum is generated from the interaction of two nuclei, and therefore carries information about the interaction. Transverse momentum has two components and can be expressed as:

$$p_T = \sqrt{p_x^2 + p_y^2}, \tag{2.1}$$

where p_x and p_y are the momentum components in the x and y directions, respectively.

2.2 Rapidity and Pseudorapidity

Rapidity characterizes the momentum component of a produced particle in the *longitudinal* or z direction. A key property of rapidity is that differences in rapidity are invariant under a Lorentz transformation in the z direction [26]. It can be expressed as:

$$y = \frac{1}{2} \ln \left(\frac{E + p_z}{E - p_z} \right), \tag{2.2}$$

where E is the total energy of the particle and p_z is the longitudinal momentum component along the beam axis (z direction).

When measuring highly relativistic particles, sometimes the total energy of the particle is not known because the mass of the particle is not always known in Equation 2.3:

$$E^2 = p^2 + m_0^2. \tag{2.3}$$

Under the limit where the speed of a particle is very close to the speed of light, the energy from the mass of the particle is approximately negligible, and $E \approx p$, so the rapidity (y) approaches the pseudorapidity. The pseudorapidity (η) can be expressed as:

$$\eta = -\ln \left[\tan \left(\frac{\theta}{2} \right) \right]. \tag{2.4}$$

The angle θ is between the particle's momentum vector direction and the z direction. Similar to rapidity, differences in pseudorapidity (η) are also Lorentz invariant [27] and this is the reason why pseudorapidity (η) is used to describe the

angle of a particle relative to the beam axis plane instead of θ, where the Lorentz transformations become more complicated.

2.3 Centrality

Centrality is used to characterize the collision geometry with respect to the impact parameter b. When $b = 0$, the centrality is 0% and this is referred to as a head on collision, since all the matter of the incoming nuclei participate in the interaction. Large values of centrality correspond to larger values of b, and therefore less matter will participate in the interaction. The impact parameter cannot be measured experimentally. Instead, the multiplicity of produced particles is used to determine the centrality [28]. This is based on the intuitive assumption that the number of particles produced in the collision increases monotonically with an increasing number of participating nucleons, and therefore with decreasing values of b. The centrality with respect to the number of produced particles is defined as:

$$c = \frac{1}{N_{events}} \int_{M_0}^{\infty} \frac{dN}{dM} dM. \tag{2.5}$$

The term M, also referred to as the multiplicity, are the number of particles produced in a heavy-ion collision. The term M_0 refers to a set of collisions with a particular multiplicity, of which the centrality c is determined. The term N_{events} represents the number of collisions, and dN/dM is the number of collisions as a function of the multiplicity M.

Figure 2.2 shows the centrality percentiles of charged particle multiplicities from Pb-Pb collisions recorded with the ALICE detector. More particles are produced for the lower centrality percentages (central collisions), and fewer particles for the higher centrality percentages (peripheral collisions). Number of events in centrality bin with same width are same. However, we can see larger multiplicity range for more central collision due to the decrease of the probability.

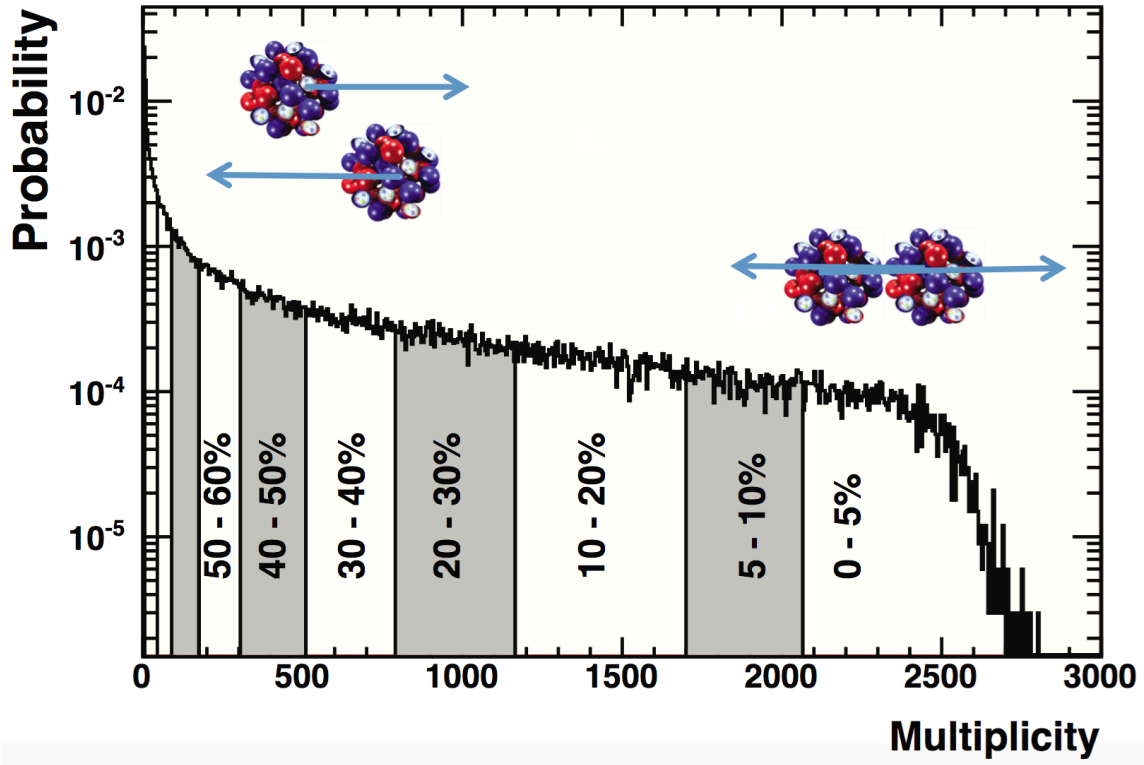

Figure 2.2: Uncorrected charged particle multiplicity distribution for Pb-Pb collisions with a center-of-mass energy per nucleon $\sqrt{s_{NN}} = 2.76$ TeV. The produced charged particles have $|\eta| < 0.8$ [5].

2.4 Eccentricity

The initial spatial eccentricity is a key parameter related to the initial geometry of the participating matter in a heavy-ion collision. It is defined as:

$$\varepsilon_2 = \frac{\left\langle \sigma_y^2 - \sigma_x^2 \right\rangle}{\left\langle \sigma_y^2 + \sigma_x^2 \right\rangle}, \tag{2.6}$$

where $\sigma_x^2 = \langle x^2 \rangle - \langle x \rangle^2$, $\sigma_y^2 = \langle y^2 \rangle - \langle y \rangle^2$, are averages of participants with respect to the distributions of nuclear matter in the overlap region of the colliding nuclei. It can be mapped to the centrality using an initial state model, which simulates a heavy-ion collision and the corresponding particle production. Figure 2.3 shows a particular calculation of ε_2 with respect to the multiplicity based centrality from the T$_{\mathrm{R}}$ENTo model (which will be discussed later). For every event in T$_{\mathrm{R}}$ENTo model simulation, we have centrality and ε_2 of that event. Therefore we can calculate the average of ε_2 for different centrality bins. The eccentricity decreases when the centrality approaches 0 %. Head on collisions have a more circular overlap region, which leads to lower values of ε_2.

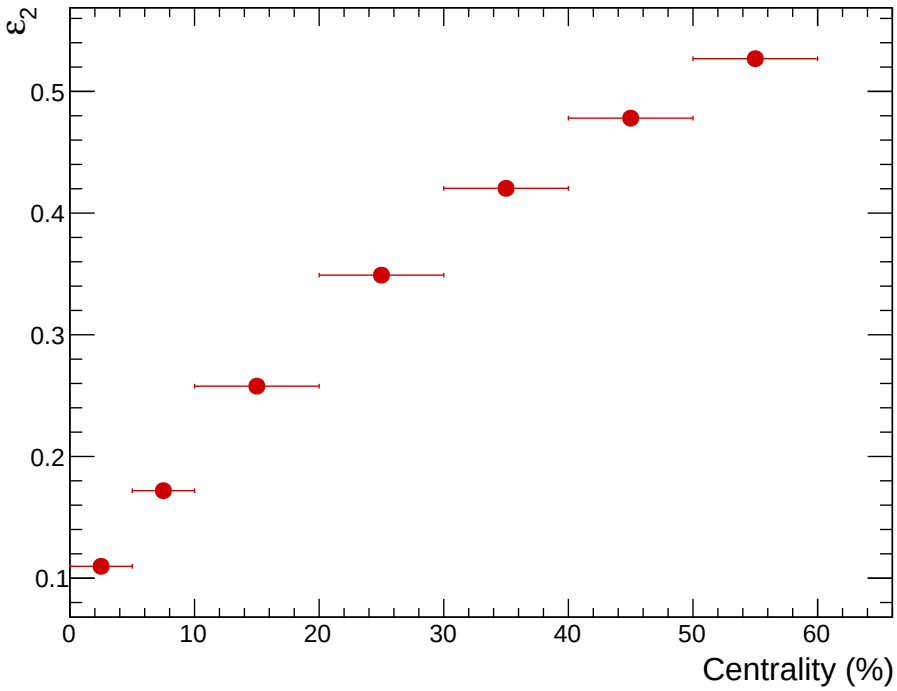

Figure 2.3: Average values of ε_2 for different centrality bins of Pb-Pb collisions from the T$_\mathrm{R}$ENTo model [6]. 500 million events were used for this simulation.

Chapter 3

Experimental Setup

In this chapter, the main aspects of the experimental setup will be introduced for the anisotropic-flow measurements presented in the subsequent chapters. A brief introduction to the Large Hadron Collider (LHC) is presented in Section 3.1. Section 3.2 describes one of the major experiments at CERN: A Large Ion Collider Experiment (ALICE). Finally a detailed description of the ALICE sub-detectors that were used in this analysis are introduced in Section 3.3.

3.1 Large Hadron Collider

The Large Hadron Collider (LHC) started operations in 2008 and is the world's highest energy particle collider. The LHC ring is located at the border of France and Switzerland. The LHC tunnel spans about 27 kilometers in circumference with accelerators positioned about 100 m beneath the earth's surface. The temperatures

achieved in heavy-ion collisions at the LHC energies can be 5.5×10^{12} K [29]. At such extreme temperatures, all composite hadrons will melt into quarks and gluons, which are the most fundamental building blocks of baryonic matter. The superconducting electromagnet rings built in the LHC accelerate protons and Pb ions so that the center of mass energies of proton-proton or Pb-Pb collisions can be up to a $\sqrt{s_{NN}}$ of 13 TeV and 5.02 TeV per nucleon, respectively.

The Pb atoms in the LHC are first fully ionized in the Electron Cyclotron Resonance (ECR) facility, and then are accelerated to an energy of 4.2 MeV/nucleon by a linear accelerator (LINAC 3). The Pb ions beam then subsequently travel to the Low-Energy Ion Ring (LEIR) and are accelerated to 72.2 MeV/nucleon. After that, they go through a series of 2 synchrotrons: the Proton Synchrotron (PS), and the Super Proton Synchrotron (SPS), in that order. Each of these synchrotrons will accelerate the beam to higher and higher energies; the PS and the SPS will accelerate the injected Pb ions to energies of 5.9 GeV/nucleon, and 176.4 GeV/nucleon, respectively. The accelerated beam will then be injected into the main LHC ring where they will reach the energy required for the experiment, which for the measurements in this thesis, is 2.76 TeV/nucleon [29].

The four major experiments within the LHC ring are: A Large Ion Collider Experiment (ALICE), A Toroidal LHC Apparatus (ATLAS), Large Hadron Collider beauty (LHCb), and the Compact Muon Solenoid (CMS). The number of a certain type of event per second, N_{event} in the LHC collisions depends on the cross section of the event σ_{event} and L which is the the luminosity of the collider:

$$N_{\text{event}} = L\sigma_{\text{event}}. \tag{3.1}$$

The luminosity depends on the properties of the particle beams, such as the density of particles in a bunch, the revolution frequency and the angle at which the two beams cross at an intersection point. The peak luminosity for the Pb-Pb collisions will be $10^{27}\text{cm}^{-2}\text{s}^{-1}$ at a bunch crossing each 100 ns within the ALICE detector, restricted by its read out time of Time Projection Chamber (TPC) [8].

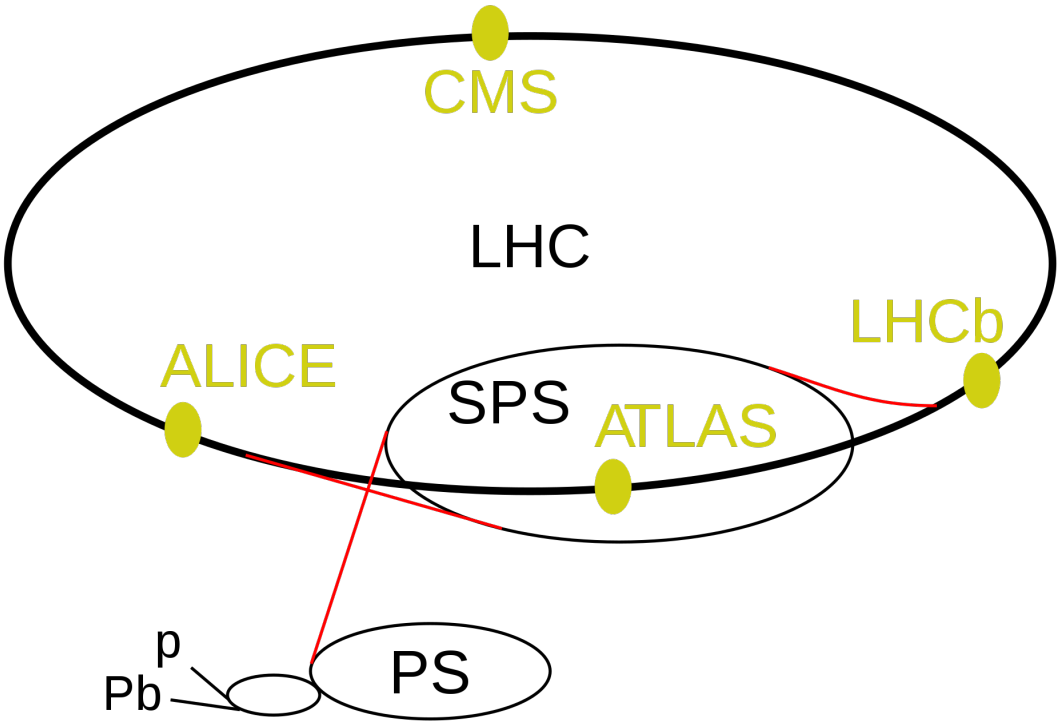

Figure 3.1: Large Hadron Collider [7].

3.2 A Large Ion Collider Experiment (ALICE)

The ALICE detector is dedicated to the study of heavy ion collisions. It is a general purpose detector designed to measure and identify hadrons, leptons and photons produced in the collision over a large momentum range, 100 MeV/$c < p_{\mathrm{T}} <$ 100 GeV/c. It is located at Point 2 in the LHC ring, the relative positions of the four main experiments are shown in Figure 3.1. The ALICE detector has three main components: the central barrel, the forward muon spectrometer, and other forward detectors. It consists of a central barrel around the interaction region inside a solenoidal magnet with a field strength of up to 0.5 T [30]. The magnet has a length of 12 m and an inner radius of 5 m. The central barrel covers the pseudorapidity range $|\eta| < 0.9$ over the full azimuthal angle (φ)

Compared to the other LHC experiments, the ALICE detector is particularly well-suited to measure particles produced from heavy-ion collisions. The ALICE detector contains 18 sub-detectors, has overall dimensions of 16×16×26 m^3 and is approximately 10,000 tons in weight. The sub-detector systems that were used in this dissertation include the Inner Tracking System (ITS), the Time Projection Chamber (TPC), and the VZERO (V0) detectors, these will be described in detail in next section.

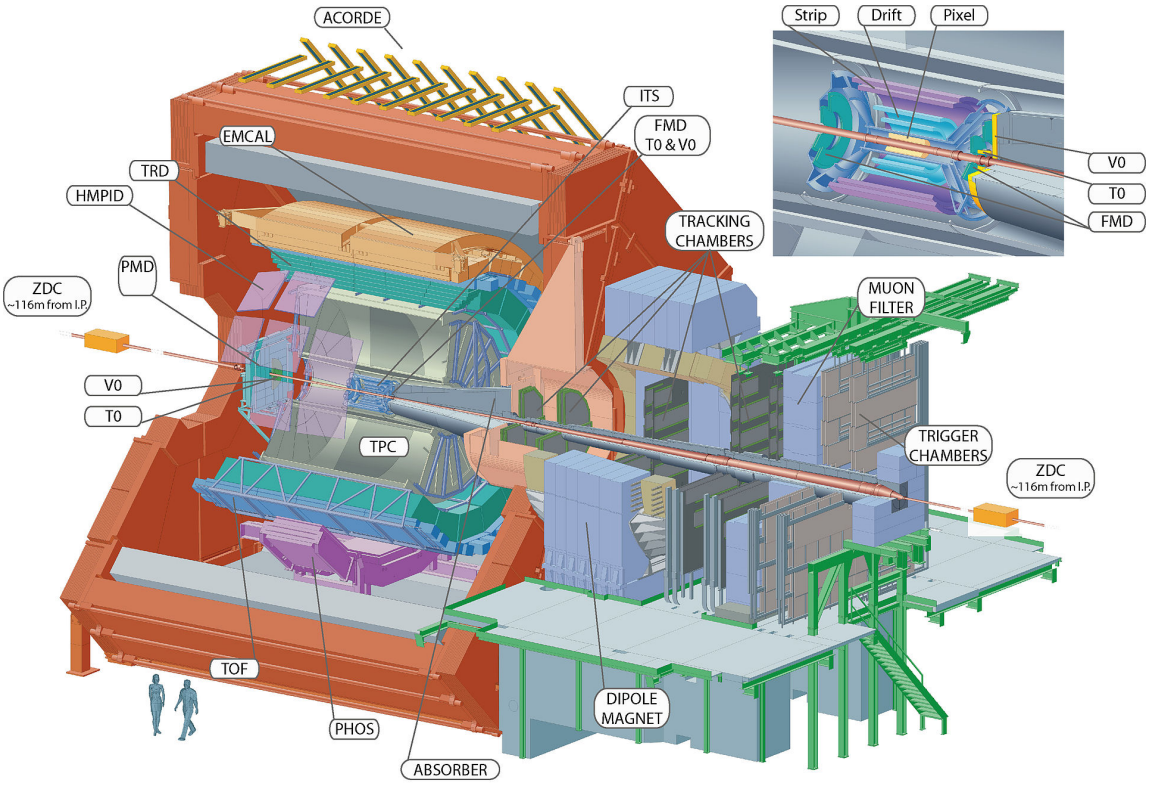

Figure 3.2: The ALICE detector [4].

3.3 Sub-detectors

3.3.1 Time Projection Chamber (TPC)

The TPC detector is the main detector used in the ALICE experiment and operates in a solenoidal magnetic field of 0.5 T. It is mainly used for tracking and momentum measurements, but can also achieve particle identification of charged particles in the momentum range from 0.5 to 10 GeV/c [31]. The TPC covers 100% of the

azimuthal angle of produced particles, and a pseudo-rapidity range of $|\eta| < 0.9$ for full tracks length within the TPC volume. Because any inefficiency in the detector's azimuthal acceptance will cause a non-negligible systematic bias for the anisotropic-flow analysis, the uniform azimuthal coverage ensures the TPC is an ideal detector for anisotropic-flow analysis.

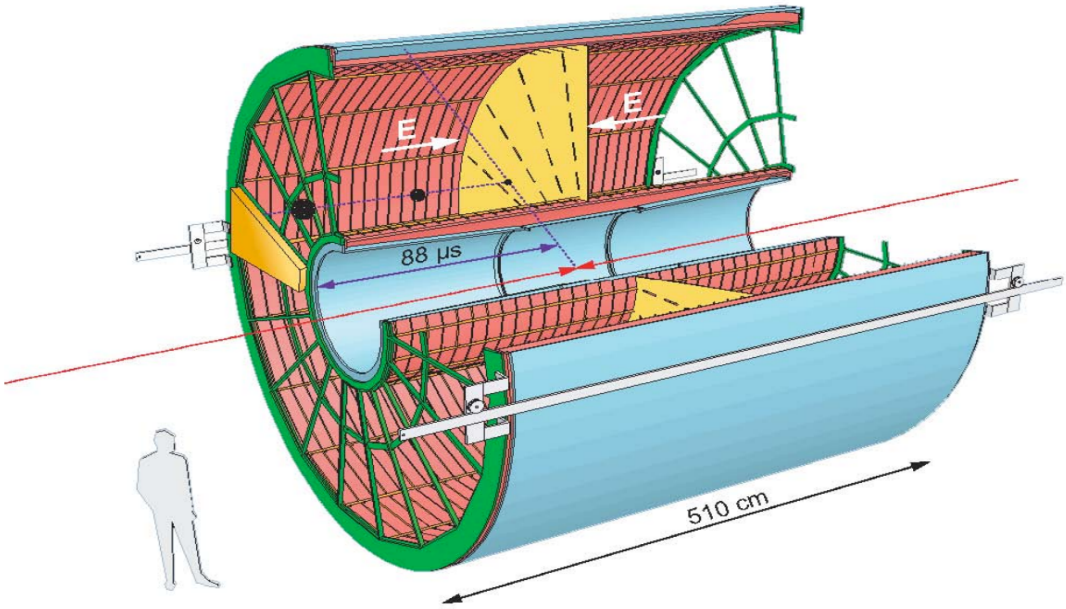

Figure 3.3: The Time Projection Chamber (TPC) [4].

Figure 3.3 shows the structure of the ALICE TPC detector. The TPC is a gaseous detector filled with 90 m^3 gas mixture of $Ne/CO_2/N_2$. The TPC gas is ionized by the charged particles from heavy ion collisions, and the liberated electrons drift towards the end plate, which is the green part in Figure 3.3. Each plate provides a maximum of 159 points along the particle path for tracking [30]. The read-out pad provides the coordinate in the x-y plane, where as the z-coordinate is calculated from the drift

time and drift velocity. The maximum drift time is approximately 88 μs.

Besides the primary usage for tracking, the TPC is also used for particle identification (PID) by measuring the ionization energy loss (dE/dx) and momentum p of the produced particles. Ionization plays a special role because it is a function of the particle velocity. As a charged particle passes through the gas mixture medium, the inelastic collisions between a produced charged particle and atoms in the gas result in ionization of the gas, which corresponds to a decrease in the particle energy. The energy loss depends on the momentum of the produced particle. The energy loss per path length is commonly described by the Bethe-Bloch formula as shown below:

$$-\frac{dE}{dx} = 4\pi N_A r_e^2 m_e c^2 p z^2 \frac{Z}{A}\frac{1}{\beta^2}\left[\frac{1}{2}\ln\left(\frac{2m_e c^2\beta^2\gamma^2 T_{max}}{I^2}\right) - \beta^2 - \frac{\delta}{2}\right], \tag{3.2}$$

where β is the relativistic particle velocity, γ is the Lorentz factor, z is the charge of the traversing particles, N_A is Avogadro's number, and I is the effective ionization potential of atom species constituting the medium. In addition, Z is the atomic number and A is the mass numbers of the atom species in the medium. As shown in Figure 3.4, the species of different particles such as electrons, pions, kaons, and protons are clearly separated by the black curves predicted by Equation 3.2. The curve indicates the expected mean energy loss.

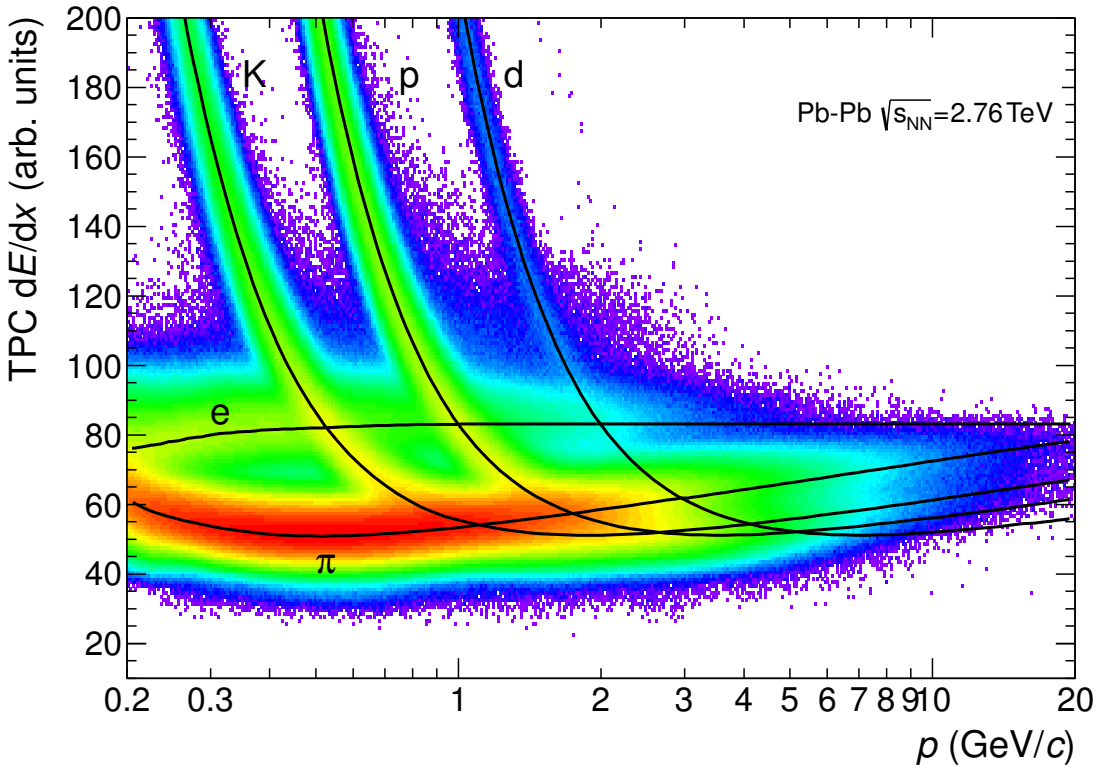

Figure 3.4: Energy-loss signal as a function of momentum measured by the TPC detector [8].

The differing particle species behavior at a given momentum can be used to identify a partuclar particle. Such a procedure is most effective for smaller values of momentum. The curvature of the track helix can determine the transverse momentum using Equation 3.3:

$$p_{\mathrm{T}} = 0.3BRq \ (\mathrm{GeV}/c), \tag{3.3}$$

where B is the magnitude of the magnatic field, R is the radius of curvature, and q is particle charge.

3.3.2 Inner Tracking System (ITS)

The Inner Tracking System (ITS) surrounds directly the beam pipe around the interaction region. The ITS can identify the primary vertex corresponding to a heavy-ion collision. This is the spatial location of the collision. It can also identify secondary vertices, which can result from beam gas collisions. It provides track and momentum determination for low momentum particles, which are less than 200 MeV/c [32] and cannot be measured by the TPC. The information from the ITS is used to improve the momentum and angular resolution of tracks reconstructed by the TPC.

The ITS is about 87.2 cm in diameter, as shown in Figure 3.5.

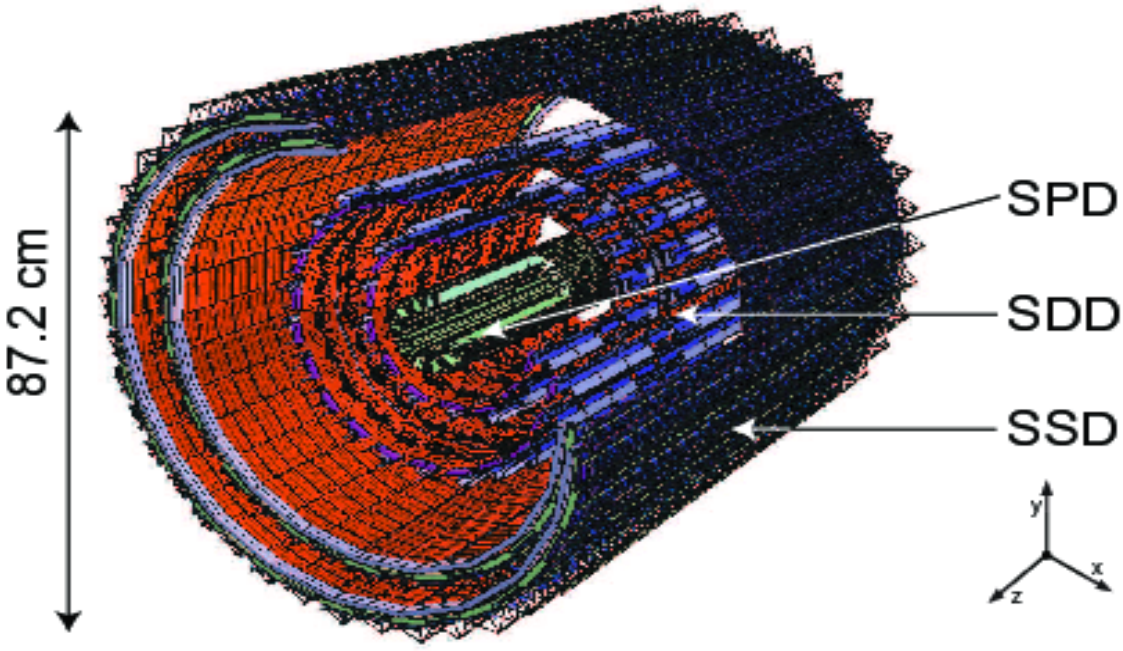

Figure 3.5: The Inner Tracking System (ITS) [9].

Table 3.1: General information on the six silicon detector layers of the ITS [20]

Layer	Type	Number of Modules	r (cm)	$\pm z$ (cm)	Resolution $r\phi \times z$ (μm)
1	pixel	80	3.9	14.1	12 × 100
2	pixel	160	7.6	14.1	12 × 100
3	drift	84	15.0	22.2	35 × 25
4	drift	176	23.9	29.7	35 × 25
5	strip	748	38.0	43.1	20 × 830
6	strip	950	43.0	48.9	20 × 830

The detector consists of 6 cylindrical layers of silicon detectors around the beam pipe which has a radius of 3 cm. The particle density close to the beam pipe can be up to 50 cm^{-2}, therefore, a high spatial resolution detector is required to distinguish individual tracks. The two innermost layers are silicon pixels detectors (SPD) fulfill these requirements and provide two dimensional hit information. The position of the primary vertex is determined from the SPD. The third and fourth layer are silicon drift detectors (SDD). They are used to determine the drift time of the charge deposited when a particle passes through the detector together with the segmentation through cathode strips to determine the position of the particle. The two outermost layers are double sided silicon strip detectors (SSD), which provide a match between the tracks reconstructed in the ITS and the TPC.

Table 3.1 shows the dimensions of the ITS detector. The SPD has a resolution of about 0.5% centrality bin width, which can be used for centrality determination. The SDD and SSD facilitate particle identification by measuring the energy loss dE/dx of charged particles produced in high-energy collisions. Figure 3.6 shows the dE/dx distribution which can be used for Particle Identification (PID) from the ITS.

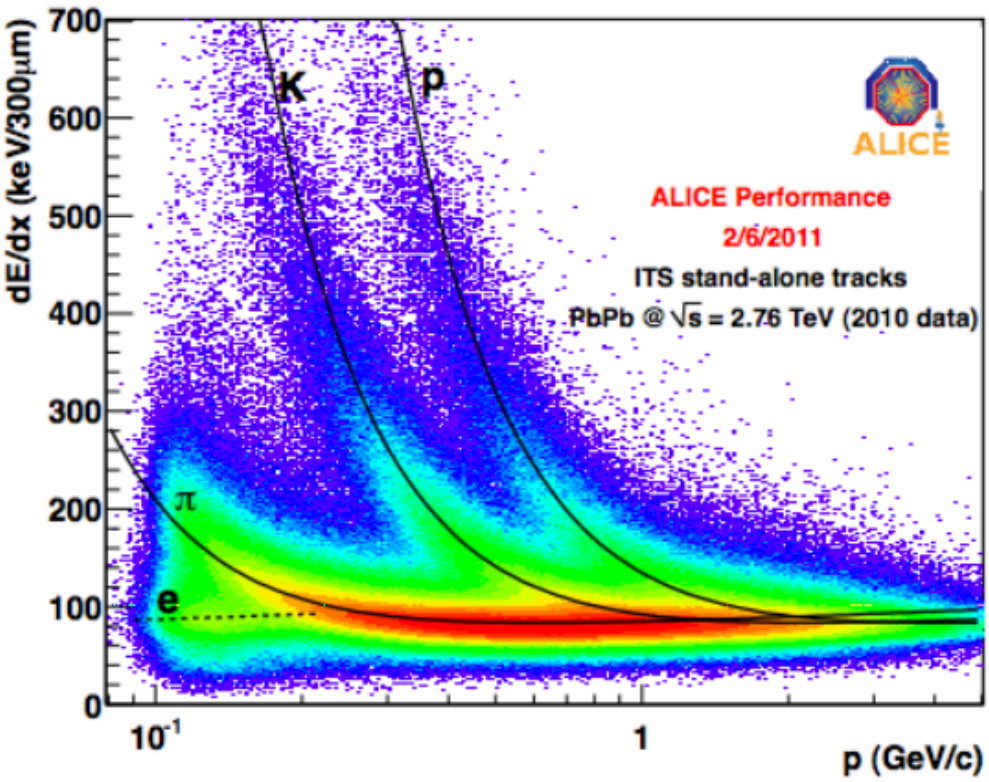

Figure 3.6: Energy-loss signal as a function of momentum measured by the ITS detector [10].

3.3.3 VZERO (V0)

The V0 detector [33] is a small-angle detector split into two arrays of scintillator counters, V0-A and V0-C. The V0 is initially used for triggering on a heavy-ion collision, which instructs the other detectors to record data when a collision has occurred. The trigger requires a coincidence signals for both the V0-A and V0-C. The V0 detector measures charged particles from a collision based on the deposited

energy of a passing particle, as the signal of a detector element is proportional to the number of particles that have traversed that element. Each sub detector is placed asymmetrically on either side of the ITS along the beam axis. The V0-C is located 90 cm from the ALICE interaction point (IP) and V0-A is 340 cm from the IP on the opposite site, as shown in Figure 3.7.

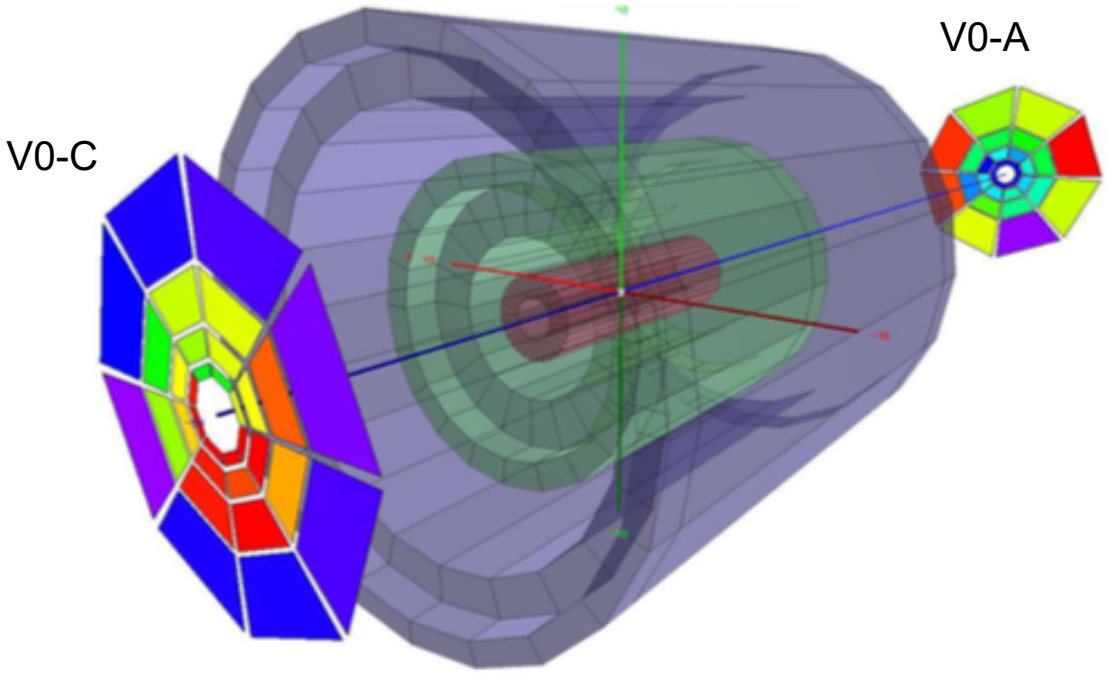

Figure 3.7: The VZERO detectors with V0-A and V0-C at the both side of ITS [11].

Each scintillator covers different pseudorapidity ranges due to the asymmetry of their positions. V0-A covers $2.8 < \eta < 5.1$ while V0-C covers $-3.7 < \eta < -1.7$. Each of the VZERO arrays is segmented into four rings, and each ring is further divided into eight sectors [34]. Table 3.2 shows the pseudorapidity and angular acceptance

Table 3.2: V0A and V0C arrays. θ measures in unit of degree [8]

Rings	V0A		V0C	
	η_{max}/η_{min}	$\theta_{min}/\theta_{max}$	η_{min}/η_{max}	$\theta_{max}/\theta_{min}$
0	5.1/4.5	0.7/1.3	-3.7/-3.2	177.0/175.3
1	4.5/3.9	1.3/2.3	-3.2/-2.7	175.3/172.4
2	3.9/3.4	2.3/3.8	-2.7/-2.2	172.4/167.5
3	3.4/2.8	3.8/6.9	-2.2/-1.7	167.5/159.8

of the four rings.

The centrality of the data analyzed in this dissertation is determined by the V0 detector. The centrality resolution in the most central collisions is about 0.5% [35].

3.4 Tracks Reconstruction and Selection

Charged track reconstruction by the ALICE software is done in several steps starting with the determination of the primary vertex, which is found from the clusters in the two SPD layers. The clusters in the central barrel are combined into tracks, which take into account the curvature approximated with a 'helix' caused by the magnetic field as well as the energy loss. Then, a reconstruction algorithm uses the Kalman filtering techniques [36] to fit these space points to obtain track candidates to reconstruct the particle kinematics. These space points are discrete signals left by charged particles when passing through the TPC tracking device (clusters).

The track finding and fitting starts from the outermost pad rows of the TPC, where the spacial separation between the tracks is the largest, progressively fits inward to the ITS. Track candidates are then assigned with different clusters using

the Kalman filter in the ITS data to improve the estimation of track parameters such as momentum. After the assignment, the ITS stand-alone tracking procedure is conducted with the leftover clusters. This is to recover the tracks that are lost in the TPC because of crossing a dead zone, decays or the momentum cut-off. The procedure is then restarted from the inner ITS layer to the outer TPC boundary after all the ITS clusters are added to the tracks. In this tracking step, improperly assigned clusters are eliminated to improve the track quality. It then finally extrapolates into the Time-of-Flight (TOF), Transition Radiation Detector (TRD), High Momentum Particle Identification (HMPID), and Photon Spectrometer (PHOS) detectors to acquire information that can be used to identify the particle species. At the final stage, the filter is once again reversed for a final refit of the track back towards the primary vertex, the best track parameters are calculated at the vertex. Secondary tracks can be used to reconstruct decay vertices. These are the tracks that failed the final refit toward the primary vertex. Figure 3.8 shows charged tracks reconstructed from a single Pb-Pb collision.

There are two types of tracks that were used in this analysis: the TPC-only tracks and hybrid tracks. The TPC-only tracks use only the TPC clusters when the tracks were reconstructed, while the hybrid tracks use both information from the TPC and ITS. A variety of track cuts are applied to select good quality tracks from the ALICE software for this analysis. Specifically, the hybrid track used the following types to ensure the uniform distribution in the η, ϕ plane:

1. Good global tracks:

- Global tracks with SPD hit(s) and an ITS refit.

2. Complementary tracks (constrained to primary vertex to improve p_T resolution):

   - Global tracks without SPD hit(s) and with an ITS refit.
   - Global tracks without ITS refit.

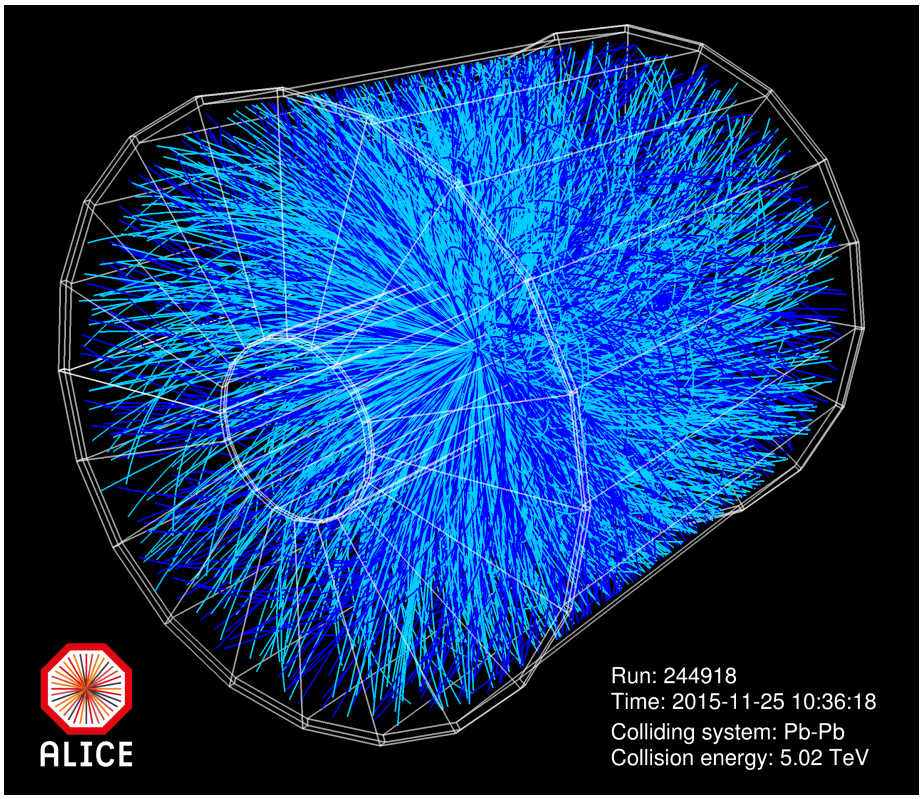

Figure 3.8: A single Pb-Pb collision from Run 244918 at the energy $\sqrt{s_{NN}} = 5.02$ TeV, recorded by the ALICE detector in November 2015 [12].

The first type gives the best transverse momentum, p_T, resolution and was used whenever available. The complementary tracks contained two categories: those with

missing hits in the SPD or those failing the refit in the ITS. They were required to be constrained to primary vertex of the corresponding events, because the transverse momentum resolution of those tracks are worse than the ones obtained from the first type. Figure 3.9 shows the azimuthal distribution of the three hybrid track categories. The figure also shows the sum of these three types of tracks in black lines, denoting a uniform acceptance in azimuthal angle.

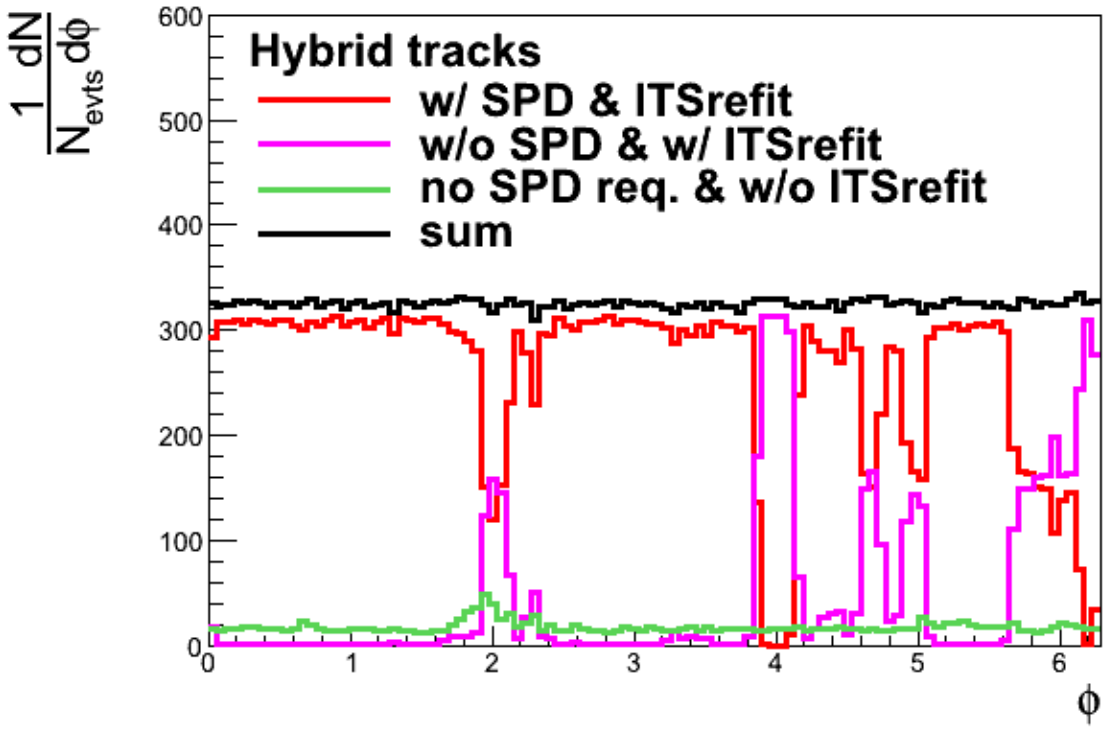

Figure 3.9: Azimuthal angle (φ) distribution of hybrid tracks in centrality class 0-10% [13].

Chapter 4

Collective Flow and Multi-particle Cumulants

4.1 Flow Harmonics

As briefly introduced in Chapter 1, anisotropic flow is a response to the initial spatial anisotropy of the system created in the heavy-ion collisions. To study the azimuthal anisotropy of produced particles, we can use Fourier expansion to decompose the azimuthal distribution relative to the symmetry planes angles. The Fourier coefficients in the decomposition also referred to as flow harmonics. [37]. Such is a decomposition of the angular distribution of produced particles is given by:

$$\begin{aligned} \frac{dN}{d\varphi} &\propto 1 + 2\sum_{n=1}^{\infty} v_n \cos[n(\varphi - \Psi_n)] \\ &\propto 1 + 2\{v_1 \cos[(\varphi - \Psi_1)] + v_2 \cos[2(\varphi - \Psi_2)] + \cdots\}, \end{aligned} \tag{4.1}$$

where φ is the azimuthal angle as defined in Chapter 2, and Ψ_n is the n-th order symmetry. The Ψ_n angle also corresponds to the direction of the anisotropic flow with order n. The flow harmonics, v_n, quantifies the magnitude of anisotropic of flow. The second and third harmonics, v_2 and v_3, represent *elliptic flow* and *triangular flow*, respectively. The second order flow tends to be the dominant component of flow in the Fourier expansion due to the initial almond shape interaction region. The third order flow is purely due to fluctuations in the initial state density, as demonstrated in Figure 4.1.

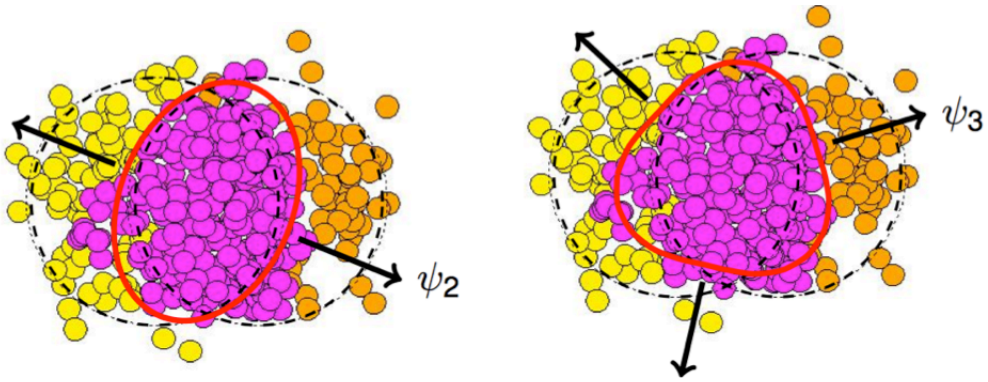

Figure 4.1: Graphic illustration of v_2 and v_3.

The nuclear matter within the interaction region in a heavy-ion collision fluctuates event by event [38]. Both types of flow are driven by anisotropic pressure gradients, which are greatest in the direction of the arrows in the Figure 4.1 (the arrows correspond to the respective Ψ_n angles). Since they are sensitive to the pressure of the medium, measurements of these types of flow can provide information of the equation of state of the quark-gluon plasma.

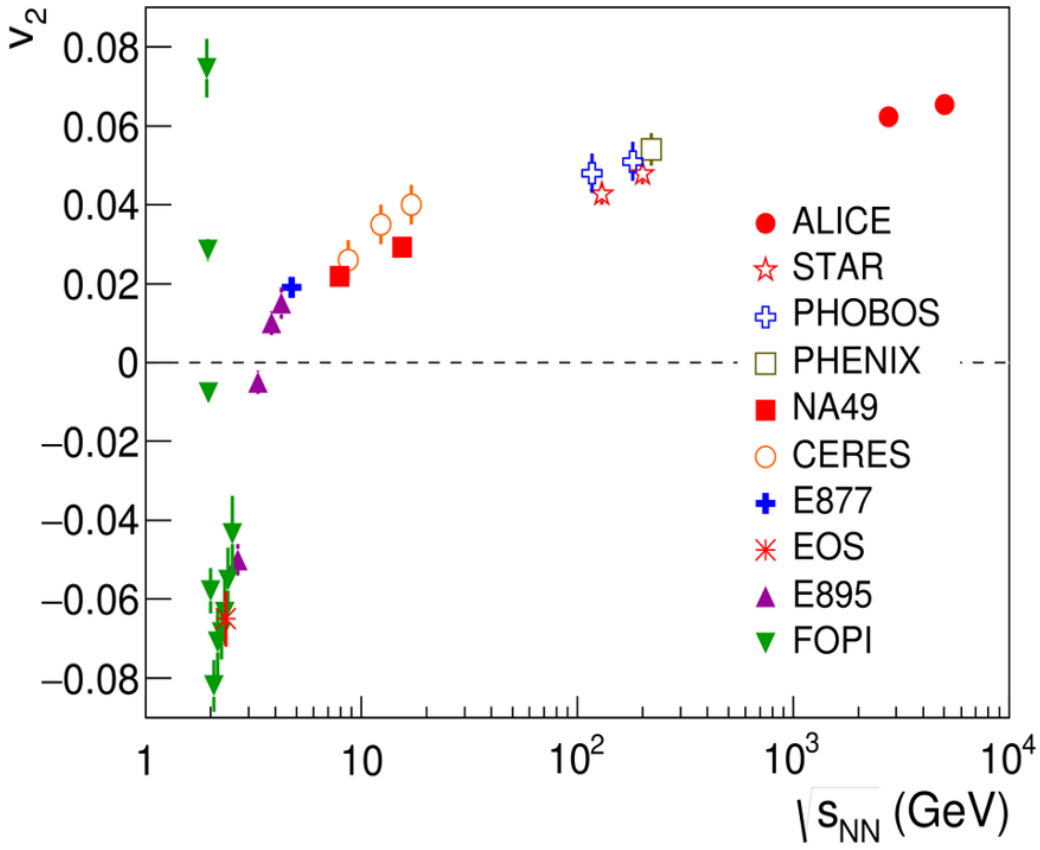

Figure 4.2: Comparison of p_T integrated v_2 at ALICE with collisions at lower energies experiments for the 20%-30% centrality range [14].

Figure 4.2 shows measurements of v_2 for different collision energies. The system lasts longer when beam energy increases, which allows more time for the development of elliptic flow. Therefore we observed that v_2 increased as the beam energy increased.

4.2 Flow Analysis Techniques

As discussed in the last section, flow harmonics can be expressed as a Fourier expansion of the azimuthal distribution. Using the orthogonality properties of the trigonometric functions in Equation 4.1 [37], the flow harmonics (v_n) can be determined from:

$$v_n = \langle \cos(n(\varphi - \Psi_n)) \rangle, \tag{4.2}$$

where Ψ_{n} is the angle of symmetry plane. The single bracket $\langle \cdots \rangle$ denotes the averaging over all the particles in an event. Since the symmetry planes are not experimentally accessible, an advanced technique called the Q-cumulant method [39] will be introduced to efficiently extract the flow harmonics without the knowledge of the symmetry-plane angle.

4.2.1 Q-cumulant Method

The Q_n-vector, which encodes the magnitude and direction of anisotropic flow, is defined as [39]:

$$Q_n \equiv \sum_{i=1}^{M} e^{in\varphi_i}, \tag{4.3}$$

where M is the multiplicity, φ_i is the azimuthal angle of i-th particle in the event. Q_n-vector has two components, Q_{nx} and Q_{ny}.

$$Q_{nx} = |Q_n| \, cos(n\Psi_n) \tag{4.4}$$

$$Q_{ny} = |Q_n| \, sin(n\Psi_n) \tag{4.5}$$

Using the Q_n-vector, the flow harmonics v_n can be expressed as:

$$v_{n\mathrm{obs}} = \frac{Re(Q_n^a Q_n^{b\,*})}{M_a\,|Q_n^b|}, \tag{4.6}$$

where M_a is the multiplicity (or number of produced particles) in a particular η range a, and b denotes η range b. "Re" refers the real part of a complex number. We use $v_{n\mathrm{obs}}$ to denote this directly calculated event-wise v_n, due to a smearing caused by the finite multiplicities. The equivalence between Equation 4.6 and Equation 4.2 is shown below:

$$\begin{aligned}
\frac{Re(Q_n^a Q_n^{b\,*})}{M_a\,|Q_n^b|} &= \frac{Re(Q_n^a |Q_n^b| e^{-in\Psi_n})}{M_a\,|Q_n^b|} \\
&= \frac{1}{M_a} Re(\sum_{i=1}^{M_a} e^{in\varphi_a^i} e^{-in\Psi_n}) \\
&= Re(\left\langle e^{in(\varphi_a - \Psi_n)} \right\rangle) \\
&= \langle \cos(n(\varphi_a - \Psi_n)) \rangle,
\end{aligned} \tag{4.7}$$

where φ_a^i is the azimulthal angle of i-th particle in η range a. The Ψ_{n} is calculated using particles in η range b and we use particles in η range a to calculate the flow harmonics. The reason for using two pseudorapidity ranges is to suppress non-flow effects. These will be discussed in next subsection.

4.2.2 Non-flow Suppression

Two-particle azimuthal correlations is a way to calculate flow harmonics v_n, and can be written as [39]:

$$\begin{aligned} v_n^2\{2\} &= c_2\{2\} \\ &= \left\langle \langle e^{ni(\varphi_1-\varphi_2)} \rangle \right\rangle \\ &= \left\langle \langle e^{ni(\varphi_1-\Psi_n-(\varphi_2-\Psi_n))} \rangle \right\rangle \\ &= \left\langle \langle e^{ni(\varphi_1-\Psi_n)} \rangle \langle e^{ni(\varphi_2-\Psi_n)} \rangle + \delta_n \right\rangle \\ &= \langle v_n^2 + \delta_n \rangle, \end{aligned} \tag{4.8}$$

where the outer bracket denotes averaging over all events, while δ_n represents the non-flow correlations [40]. We can note that the non-flow contributions are the correlations which are not correlated from the symmetry plane. They come from few-particle correlations, such as resonances, jets, and track splitting, which are not due to the anisotropic expansion of the QGP. To avoid the systematic bias in anisotropic-flow measurements introduced by non-flow, we can apply a η-gap in the calculation of flow harmonics. If the correlations are from two different η ranges, they are less likely to be short range correlations, which are the main part of non-flow. Figure 4.3 demonstrates how non-flow is suppressed by applying η-gap.

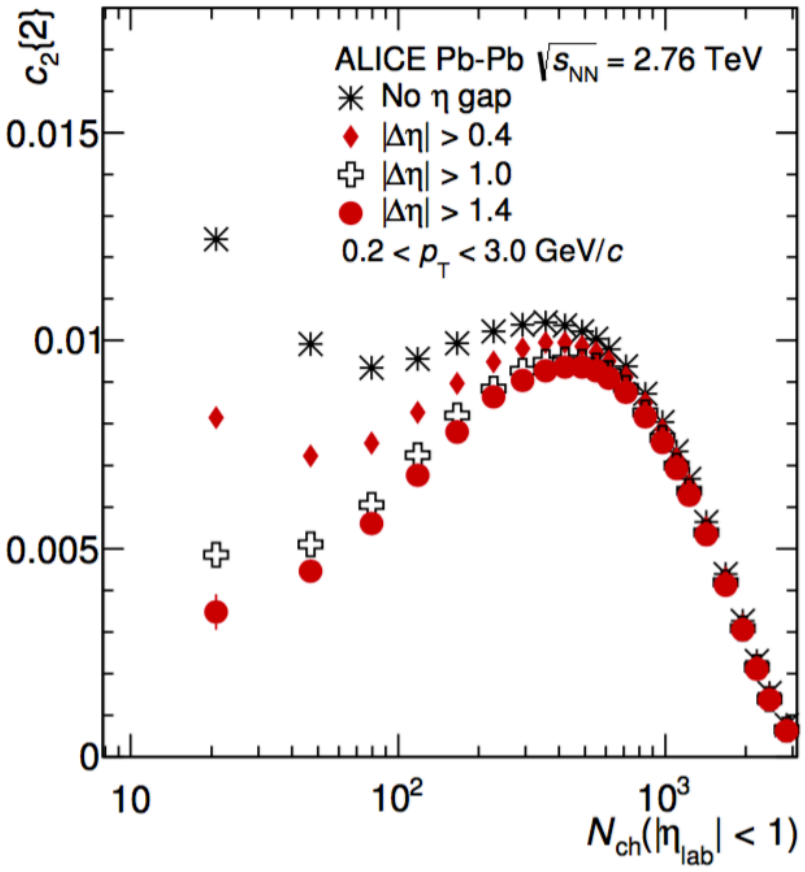

Figure 4.3: Measurement of $c_2\{2\}$ as a function of multiplicity in ALICE Pb-Pb collisions $\sqrt{s_{NN}} = 2.76$ TeV [15].

The variable, N_{ch}, is the total multiplicity, $c_2\{2\}$ represents two-particle cumulants as shown in Equation 4.8. This flow analysis with various η-gaps was carried out by the ALICE collaboration [15]. In the lower multiplicity range, the differences in flow values indicate that $c_2\{2\}$ is mainly driven by the contribution from non-flow effects. In addition, we can see that increasing the η-gap decreases the elliptic

flow value for a given multiplicity. This is expected because the tracks from non-flow contributions such as jets and resonances have smaller relative angles, which is suppressed by η separation.

Multi-particle cumulants [39], such as four-particle cumulants ($c_n\{4\}$) and 6-particle cumulants ($c_n\{6\}$), can also suppress non-flow. The relation between v_n and multi-particle cumulants [41, 42] are shown in the equations below:

$$c_n\{2\} = \langle 2 \rangle \tag{4.9}$$

$$c_n\{4\} = \langle 4 \rangle - 2 \cdot \langle 2 \rangle^2 \tag{4.10}$$

$$c_n\{6\} = \langle 6 \rangle - 9 \cdot \langle 2 \rangle \langle 4 \rangle + 12 \cdot \langle 2 \rangle^3, \tag{4.11}$$

where $\langle k \rangle$ is $\langle v_n^k \rangle$ and the single bracket is averaging over all events. From the relation, we can learn that cumulants can also quantify the nature of v_n fluctuations event by event, which we will discuss more in the next subsection. The flow harmonics from each of the cumulants are:

$$v_n\{2\} = \sqrt{c_n\{2\}} \tag{4.12}$$

$$v_n\{4\} = \sqrt[4]{-c_n\{4\}} \tag{4.13}$$

$$v_n\{6\} = \sqrt[6]{\frac{1}{4} c_n\{6\}}. \tag{4.14}$$

The following proportionality relation describes the effect of non-flow on cumulants [25]:

$$(c\{m\})_{\text{nonflow}} \propto \frac{1}{M^{m-1}}. \tag{4.15}$$

This relation is valid with the assumption that large multiplicity events are a superposition of low multiplicity events. Figure 4.4 shows the ALICE measurement of $v_2\{2\}$

and $v_2\{4\}$ for all charged and same charge particles. v_2 from fitting q-distributions (FQD) and the Lee-Yang Zeroes (LYZ) method is also provided for comparison. The non-flow contribution in $v_2\{2\}$ is larger than the non-flow contribution in $v_2\{4\}$, which leads a larger value for $v_2\{2\}$. v_2 (same charge particles) is slightly smaller than v_2 (all charge particles) because non-flow correlations are sometimes from pairs of particles with opposite charges (e.g, resonances).

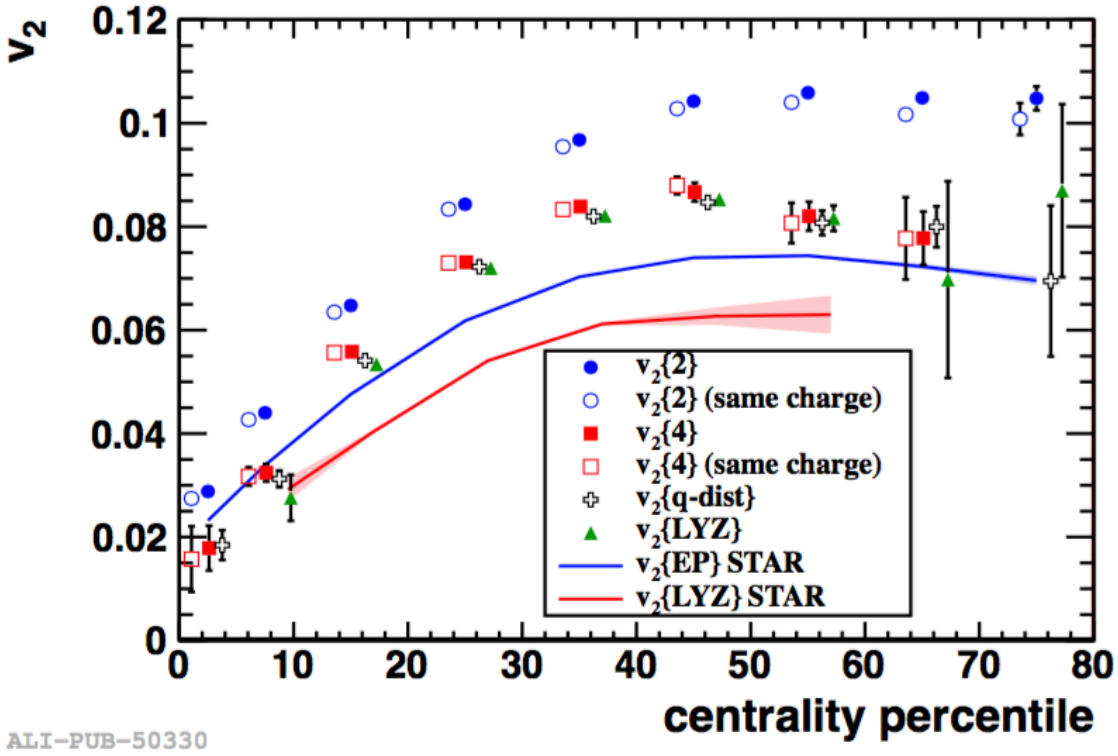

Figure 4.4: Measurement of $v_2\{2\}$ and $v_2\{4\}$ with respect to centrality. Similar sensitivity to non-flow is observed for $v_2\{\text{q-dist}\}$ and $v_2\{\text{LYZ}\}$ as compared to the $v_2\{4\}$ [5].

4.3 Fluctuations

4.3.1 Eccentricity Fluctuations

Event-by-event fluctuations in the position of participating nuclear matter during the heavy-ion collision can lead to a fluctuations of ε_n in participant plane coordinate system. As shown in Figure 4.5, the coordinate system defined by the impact parameter and the beam direction is the reaction plane coordinate system. The principal axes of the participant zone will define the participant plane coordinate system.

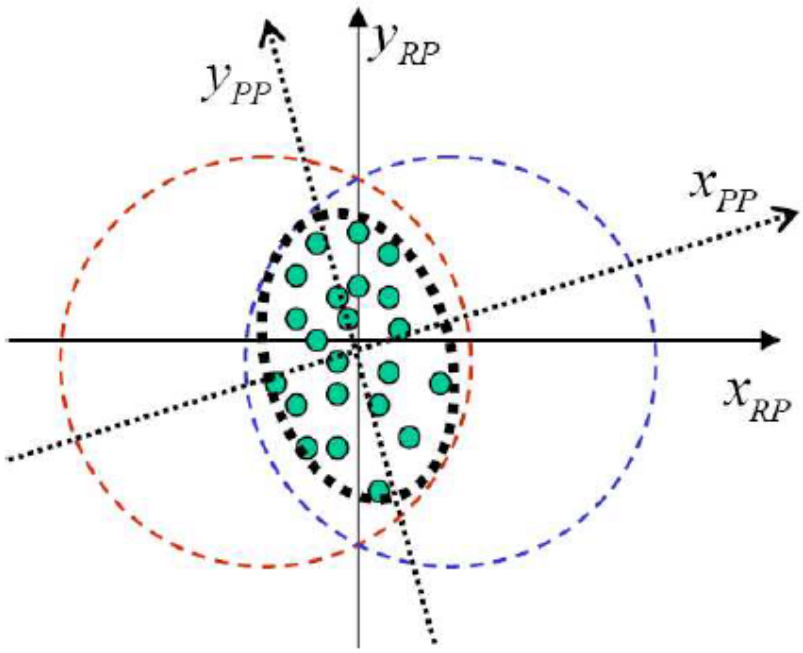

Figure 4.5: The definition of reaction plane and participant plane coordinate systems [16].

The following equation shows a Bessel Gaussian distribution, which was previously proposed to model of eccentricity fluctuations: [16]:

$$p(\varepsilon_n) = \frac{\varepsilon_n}{\sigma^2} I_0(\frac{\varepsilon_0 \varepsilon_n}{\sigma^2}) exp(-\frac{\varepsilon_0^2 + \varepsilon_n^2}{2\sigma^2}) \tag{4.16}$$

where ε_n is the eccentricity in participant plane, ε_0, is eccentricity in reaction plane, and σ controls the magnitude of eccentricity fluctuations.

A newly proposed model called Elliptic Power distribution [17] is shown below:

$$p(\varepsilon_n) = \frac{2\alpha\varepsilon_n}{\pi}(1-\varepsilon_0^2)^{\alpha+\frac{1}{2}} \int_0^\pi \frac{(1-\varepsilon_n^2)^{\alpha-1} d\varphi}{(1-\varepsilon_0\varepsilon_n cos\varphi)^{2\alpha+1}}, \tag{4.17}$$

where α related to number of sources that contribute eccentricity, ε_n and ε_0 are eccentricity in participant plane coordinate and reaction plane coordinate. One of the problems for the Bessel Gaussian distribution is the eccentricity can be larger than 1, however the eccentricity should be bound between 0 to 1 by definition. The Elliptic Power distribution by definition constrains the eccentricity between 0 to 1, which indicates that it can be a more realistic description of eccentricity fluctuations. When n is odd, ε_n is solely due to fluctuation and ε_0 will be zero. The Elliptic Power distribution reduces to a Power distribution [17] as shown in Equation 4.18:

$$p(\varepsilon_n) = 2\alpha\varepsilon_n(1-\varepsilon_n^2)^{\alpha-1}. \tag{4.18}$$

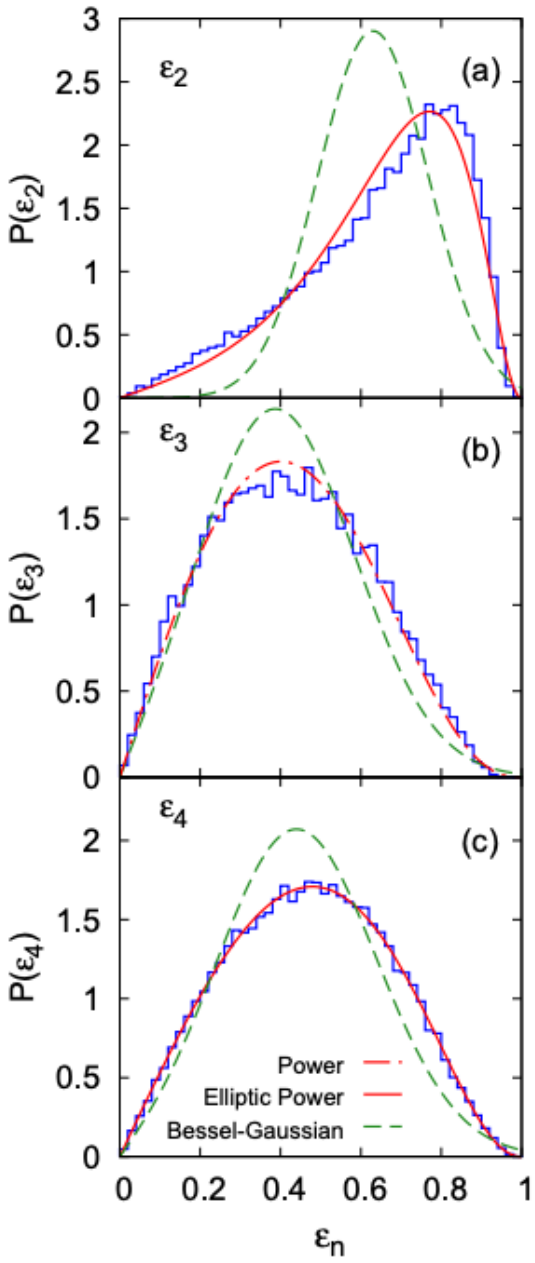

Figure 4.6: Distribution of ε_n in 75-80% central Pb-Pb collisions with Bessel Gaussian, Power, Elliptic Power distribution. (a): ε_2, (b): ε_3, (c): ε_4. Histograms are Monte Carlo Glauber simulations [17].

Figure 4.6 compares different fits to eccentricity distributions from the Monte-Carlo Glauber initial state model. The Elliptic Power distribution (red solid line) generally works better than the Bessel Gaussian distribution (green dash line).

4.3.2 Flow Fluctuations

Many hydrodynamic simulations [43–45] have proved that the flow v_n correlates almost linearly with the initial state eccentricity ε_n. Therefore, v_n can be written as::

$$v_n \approx \kappa_n \varepsilon_n, \tag{4.19}$$

where κ_n is a proportionality constant that contains all the information about the hydrodynamic response to the initial anisotropy for flow harmonic, v_n.

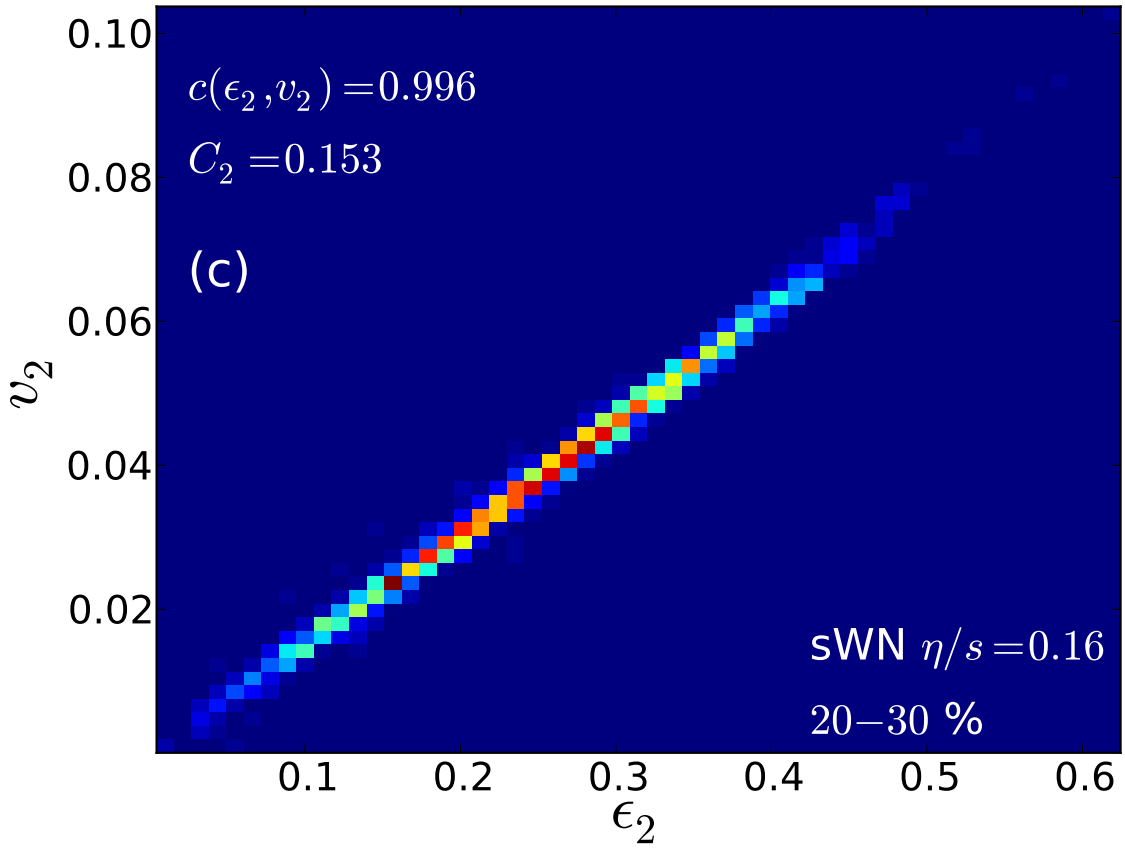

Figure 4.7: The correlation between ε_2 (initial state) and v_2 (final state) from hydrodynamic calculation [18].

Figure 4.7 demonstrates such a linear relation between the initial state eccentricity, ε_2, and final state anisotropy, v_2.

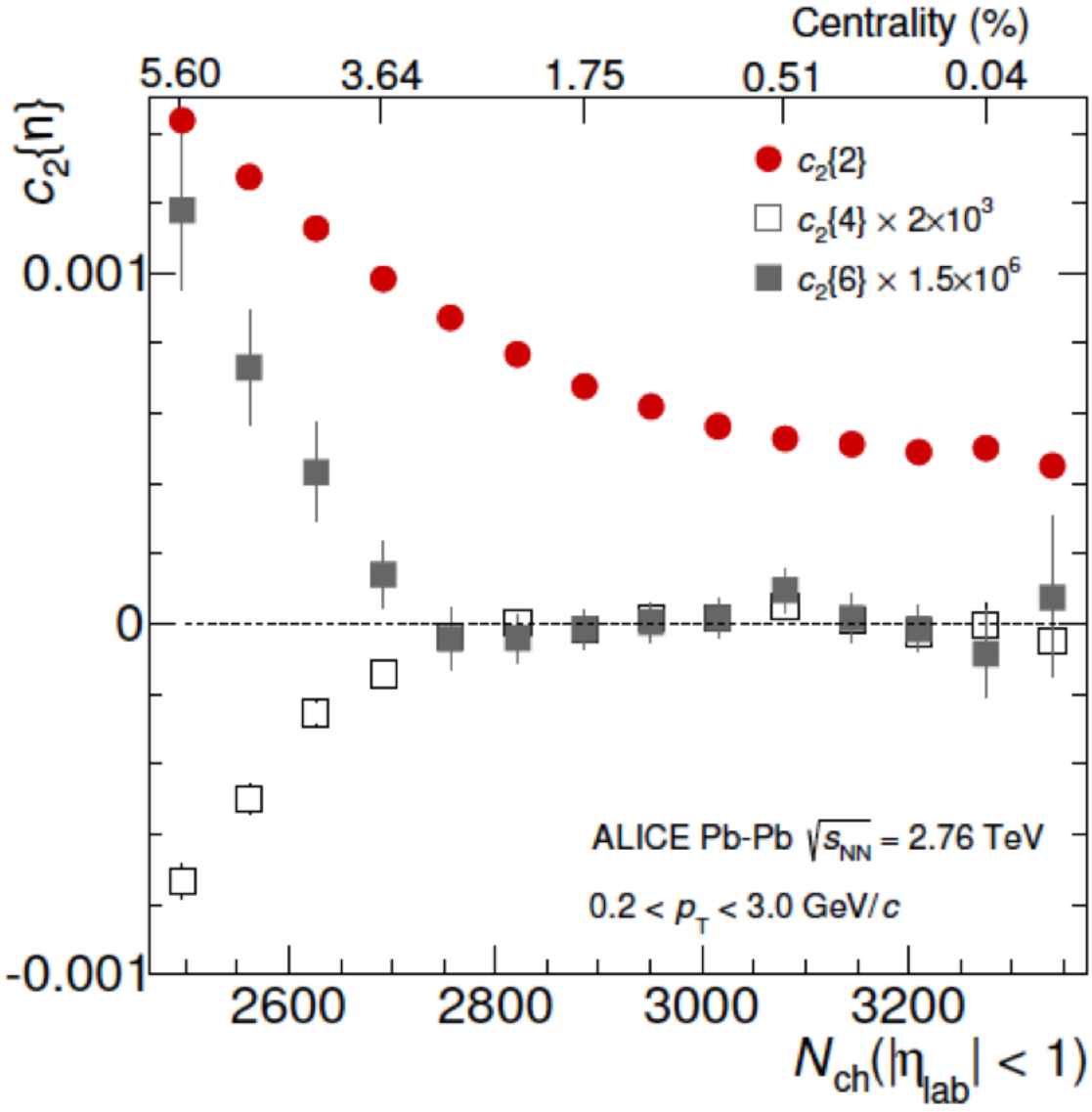

Figure 4.8: Measurement of $c_2\{2\}$, $c_2\{4\}$ and $c_2\{6\}$ at central collision [15].

Finally, in Figure 4.8, we can observe that $c_2\{2\}$ is non-zero in very central collisions, while $c_2\{4\}$ and $c_2\{6\}$ are consistent with zero. As mentioned in the last subsection, cumulants can quantify the nature of fluctuations of the flow harmonics.

In the remainder of this dissertation, this reason why the $c_2\{4\}$ and $c_2\{6\}$ go from being non-zero to zero in very central collisions will be investigated. To do this, the full v_2 distribution will be obtained using an unfolding method. These distributions can be directly compared to the Bessel Gaussian and Elliptic Power distributions, with the hope we can learn more about flow fluctuations for these very central collisions. Chapter 6 will describe such methods.

Chapter 5

Analysis Details

5.1 Analysis Software

ROOT [46], a common software package developed at CERN for data analysis for many high energy physics experiments, is used for analysis in this dissertation. This software framework is written in the C++ language and is suitable for experimental high-energy physics-data analysis. It offers an integrated I/O , an efficient hierarchical object stored with a complete set of object containers, and a C++ interpreter. The ALICE offline framework AliRoot is built on top of ROOT. It provides a full set of features needed for event generation, detector simulation, event reconstruction, data acquisition, and data analysis.

5.2 Data Taking

The data used for this analysis was recorded by the ALICE experiment in the year 2011 during the LHC run 1 period. The data processing from the ALICE detector and event reconstruction [47] serves to create the output file in the Event Summary Data (ESD) format. The numerous particles created in the Pb-Pb collisions are stored event-by-event for analysis in the Analysis Object Data (AOD) format. The AOD is a compressed file which contains the most important physical observables from the particles produced in an event, made from filtered ESD files.

There are three passes before raw data is ready to be analyzed. The first pass ensures data quality with the Online Calibration Data Base (OCDB) and quality assurance (QA) analysis. Then the reconstructed tracks are stored in the second pass, which produces the ESD files. The ESD files contain the run number, event number, trigger word, primary vertex, version of the reconstruction, array of ESD tracks, and array of reconstructed secondary vertexes [47]. A third pass runs on the ESD files to create the AOD files. These files are optimized for the physics analysis. The trigger configuration that has been used in this dissertation for the 2011 data (LHC11h/AOD145) is the kCentral trigger. The minimum bias trigger kMb records heavy-ion collisions independent of the event multiplicity. The kCentral trigger just records events with a high multiplicity which corresponds to head-on heavy-ion collisions using information from the ITS.

Table 5.1 shows the event statistics for past and future runs. The Barrel Tracking Upgrade (BTU) is anticipated for running period three to upgrade the ITS and TPC

Table 5.1: Event statistics for past and future heavy-ion running period

Running period	Years	Approx. amount of data collected/anticipated
1	2010-2013	10^7 Pb-Pb events
2	2015-2019	10^8 Pb-Pb events
3	2021-2023	10^10 Pb-Pb events

detectors. The ITS's detector tracking resolution will be improved by a factor of 3 or larger due to greater segmentation of the ITS hits [48].

5.3 Particle and Event Selection

5.3.1 Kinematic Region

Charged particles were selected from the transverse momentum interval $0.2 < p_{\mathrm{T}} < 3$ GeV/c and pseudorapidity range $|\eta| < 0.8$. When the transverse momentum was below 200 MeV/c, the tracking capability of the ALICE detector droped significantly because the low-p_{T} tracks do not make it into the TPC due to the magnetic field. The upper p_{T} boundary was set to 3 GeV/c in order to suppress non-flow correlations coming from high energy jets. The pseudorapidity range was chosen because of the uniform acceptance of the TPC in this pseudorapidity range.

5.3.2 Primary Vertex Cut

The primary vertex position in ALICE was determined with the innermost part of ITS, the SPD. The resolution in the z-coordinate is at level of 10 μm in heavy-ion

collisions, and at the level of 150 μm in proton-proton collisions. Only events with a primary vertex found in $|z| < 10$ cm were used in this analysis. The track acceptance becomes compromised for larger $|z|$ values.

5.3.3 Centrality Cut

The default estimator for centrality determination in ALICE was obtained from the measured multiplicity in the VZERO detectors. As mentioned, the resulting resolution in centrality determination based on the multiplicity in the VZERO detectors was about 0.5% for the centrality range 0-20%. In this analysis, a centrality range of 0-5% was analyzed.

5.3.4 DCA Cut

When the combined ITS and TPC information was used in the reconstruction, as in this analysis, tracks with distance of closest approach (DCA) to the primary vertex were rejected if the distance was larger than 0.3 cm, both in the longitudinal (z) and radial (xy) direction. With DCA cut, the contribution from secondary particles originating from either weak decays or from the interaction of particles with the material was minimized.

5.3.5 TPC and ITS Cut

The tracks were required to have at least 70 reconstructed space points out of the maximum 159 in the TPC and were required to have a hit in at least two out of the six ITS layers. Tracks with a smaller number of space points may results from split tracks i.e. one charged particle was reconstructed as two tracks.

When all the cuts above were placed, 4.5 million events remained for analysis from the 2011 dataset from Pb-Pb collisions with 0-5 % centrality. Figure 5.1 compares the number of events before and after centrality and the primary vertex z cut with respect to centrality. We divided these events into five centrality bins in this analysis.

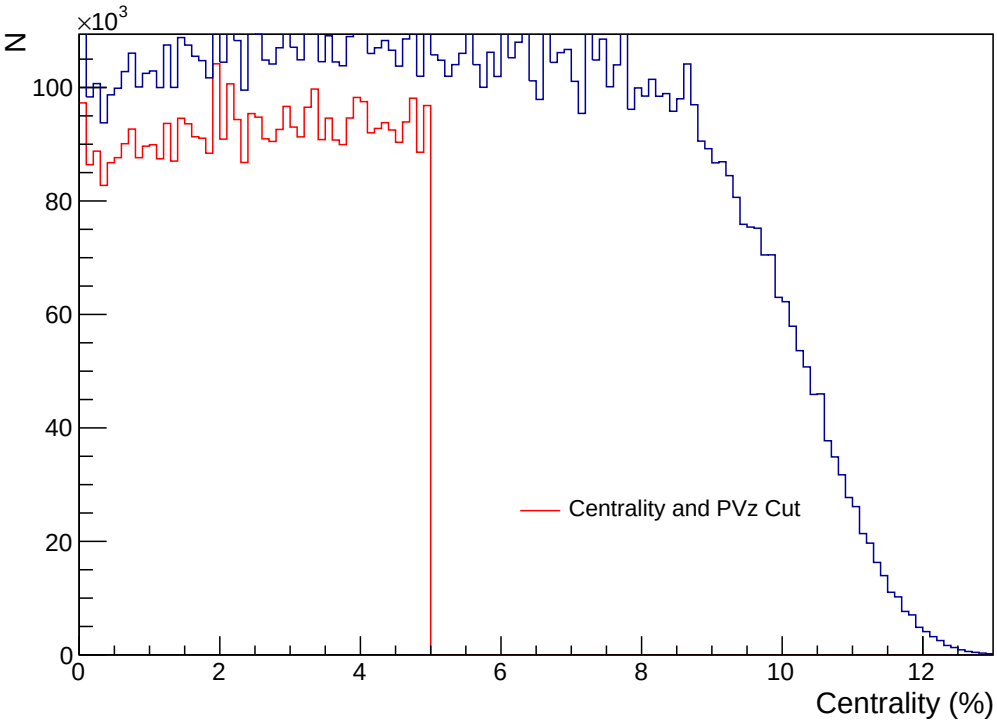

Figure 5.1: Comparions of number of events before and after centrality and PVz cut. Blue line is the data before cut, red line is the data after cut.

Chapter 6

Unfolding

The RooUnfold framework [49] contains a Bayesian unfolding procedure, and can be installed in the ROOT framework. The Bayesian unfolding procedure with RooUnfold was used in this dissertation.

6.1 Unfolding Procedure

Due to a finite number of particles in final state, a direct calculation of the v_2 distribution using Equation 4.6 was smeared, and did not truly represent the underlying v_2 distribution. Figure 6.1 illustrates the directly extracted $v_{2\mathrm{obs}}$ distribution using Equation 4.6. The underlying true v_2 should be positive for all events, but the observed v_2 was negative for nearly half of the events in the Pb-Pb 0-1% centrality class.

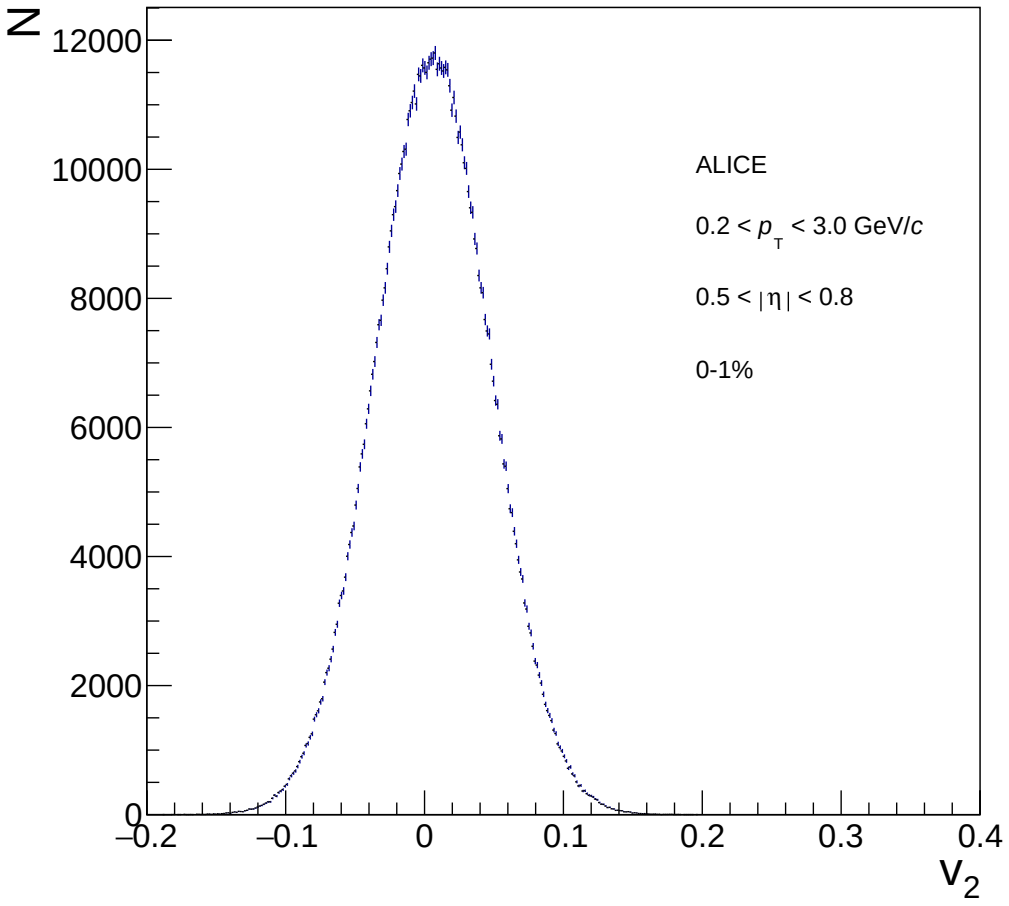

Figure 6.1: Measurement of $v_{2\text{obs}}$ of 0-1% centrality.

To extract the true v_2 distribution from this observed v_2 distribution, we utilized the Bayesian unfolding method to estimate the true v_2 distributions. To perform the unfolding procedure, a response matrix $A_{ji} \equiv p(e_j|c_i)$ is also required, where $\hat{c}$ represents the distribution of true v_2 , $\hat{e}$ represents the distribution of $v_{2\text{obs}}$ and i,j

are the indices of bins. The relation between $\hat{c}$ and $\hat{e}$ is: [50]:

$$M_{ij}^{iter} = \frac{A_{ji}c_i^{iter}}{\sum_{m,k} A_{mi}A_{jk}c_k^{iter}} \tag{6.1}$$

$$\hat{c}^{iter+1} = \hat{M}^{iter}\hat{e}. \tag{6.2}$$

In Equation 6.1, a prior $\hat{c}^0$, which is an initial estimate of the true v_2 distribution was provided and $\hat{M}$ is the backward matrix. Then $\hat{M}^0$ was calculated, and we obtained $\hat{c}^1$ using Equation 6.2. The process went through iterations to recover the true v_2 distribution. Although more iterations reduced the dependency on the prior, statistical fluctuations may introduce unwanted artifacts in the unfolded distribution. 50 iterations achieved such a compromise, and this number was used for all of the unfolded distributions shown in this dissertation.

As discussed in Chapter 4, flow fluctuations arose from a linear response to eccentricity fluctuations. Therefore, this leads to:

$$\begin{aligned} P(v_2) &= \frac{d\varepsilon_2}{dv_2}p(\varepsilon_2) \\ &= \frac{1}{\kappa_2}p(\frac{v_2}{\kappa_2}). \end{aligned} \tag{6.3}$$

Once κ_2 was known, the v_2 distribution was obtained from the ε_2 distribution or vice versa. Equation 4.18 is the reduced form of the Elliptic Power distribution with $\varepsilon_0 = 0$. Although ε_0 maybe not be zero, this Power distribution given in Equation 4.18 was used as an estimate of the ε_2 distribution for the prior with Equation 6.3. It was estimated from the following distribution:

$$P(v_2) = \frac{2\alpha v_2}{\kappa_2^2}(1 - \frac{v_2^2}{\kappa_2^2})^{\alpha-1}. \tag{6.4}$$

The κ_2 value used was 0.26, which arose from hydrodynamic calculations for the 0-5% centrality, and α was chosen to ensure $\langle v_2^2 \rangle$ calculated from Equation 6.4 roughly matches the data.

6.2 Response Matrix

The response matrix provides a map between the true v_2 and $v_{2\text{obs}}$ values. A Monte-Carlo method was used to build response matrices for different centrality bins. Although we applied an η gap to suppress non-flow, it was not fully removed. Therefore, we needed to introduce additional non-flow effects into the response matrices. The steps to build a response matrix for a certain centrality bin are as follows:

1. We randomly picked a true v_2 from $[0, 0.2]$ and a second order symmetric plane azimuthal angle from $[0, 2\pi)$.

2. We obtained the ideal azimuthal angle distribution with: $\frac{dN}{d\varphi} \propto 1+2v_2 \cos[2(\varphi - \Psi_2)]$. Only second order flow harmonics was considered when we calculated v_2 because of the orthogonality properties of the trigonometric function.

3. We filled the azimuthal angle randomly with this distribution using multiplicities from data, both in the [-0.8, -0.5] and [0.5, 0.8] η ranges. We filled a particle in the same direction as the last particle for every k particles to introduce non-flow. The determination of k will be discussed later.

4. We used Equation 4.6 to get observed single-particle flow, $v_{2\text{obs}}$. We filled the true v_2 and $v_{2\text{obs}}$ into a 2-d histogram.

5. We repeated the steps 100 million times to get the response matrix.

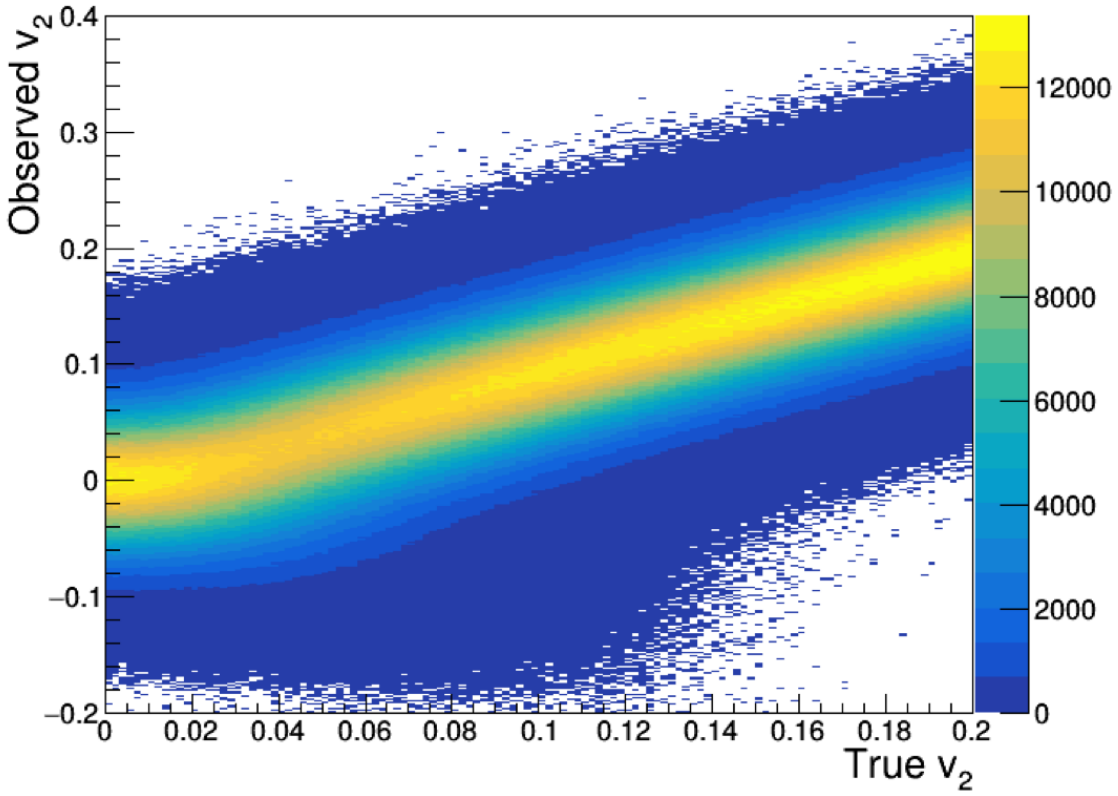

Figure 6.2: Response matrix of 0-1% centrality bin with $k = 16$. 120 bins for true v_2 between $[0, 0.2]$ and 400 bins for observed v_2 between $[-0.2, 0.4]$.

Figure 6.2 shows the response matrix for the 0-1% centrality bin. Non-flow shifts the mean of the observed v_2 to lower values, and broadens the width of the observed v_2 distribution for a given true v_2 value. This is shown in Figure 6.3:

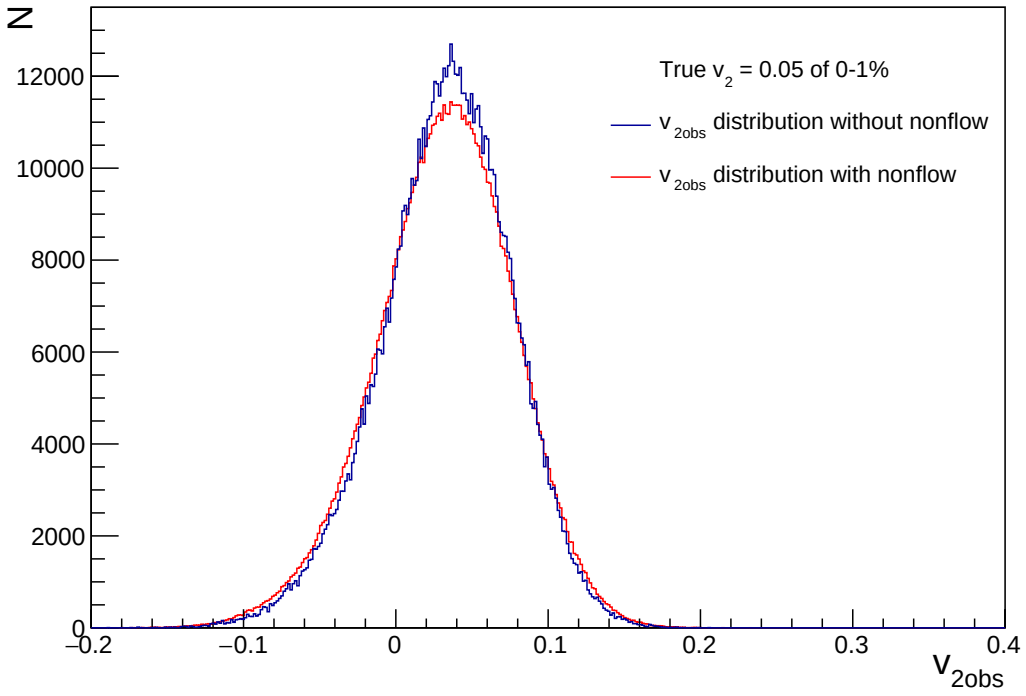

Figure 6.3: Comparison of $v_{2\text{obs}}$ with and without non-flow.

To determine k, a refolding process was carried out. Consider the following equation:

$$A\hat{c} = \hat{e}. \tag{6.5}$$

When the unfolding result $\hat{c}$ was calculated, one way to check the result is by refolding it, and checking the consistency between the refolded result $\hat{e}_{\text{refold}}$ and $\hat{e}$.

$$\hat{e}_{\text{refold}} = A\hat{c}_{\text{unfold}} \tag{6.6}$$

The amount of non-flow k is a free parameter in response matrix, and we choose k to ensure that $\hat{e}_{\text{refold}}$ and $\hat{e}$ matched as well as possible. Table 6.1 shows the

Table 6.1: Best k for 0-5% centrality bins

Centrality Bin	0-1%	1-2%	2-3%	3-4%	4-5%
k	16	16	18	20	21

optiminal k for each centrality bin in the 0-5% centrality range. With these k values, the difference between refolding v_2 and $v_{2\text{obs}}$ was minimized. The comparison of the refolded v_2 distribution and the $v_{2\text{obs}}$ distribution in different centrality bins is shown in Figure 6.4 - 6.8. The refolded v_2 and $v_{2\text{obs}}$ distributions were consistent for all the centrality bins.

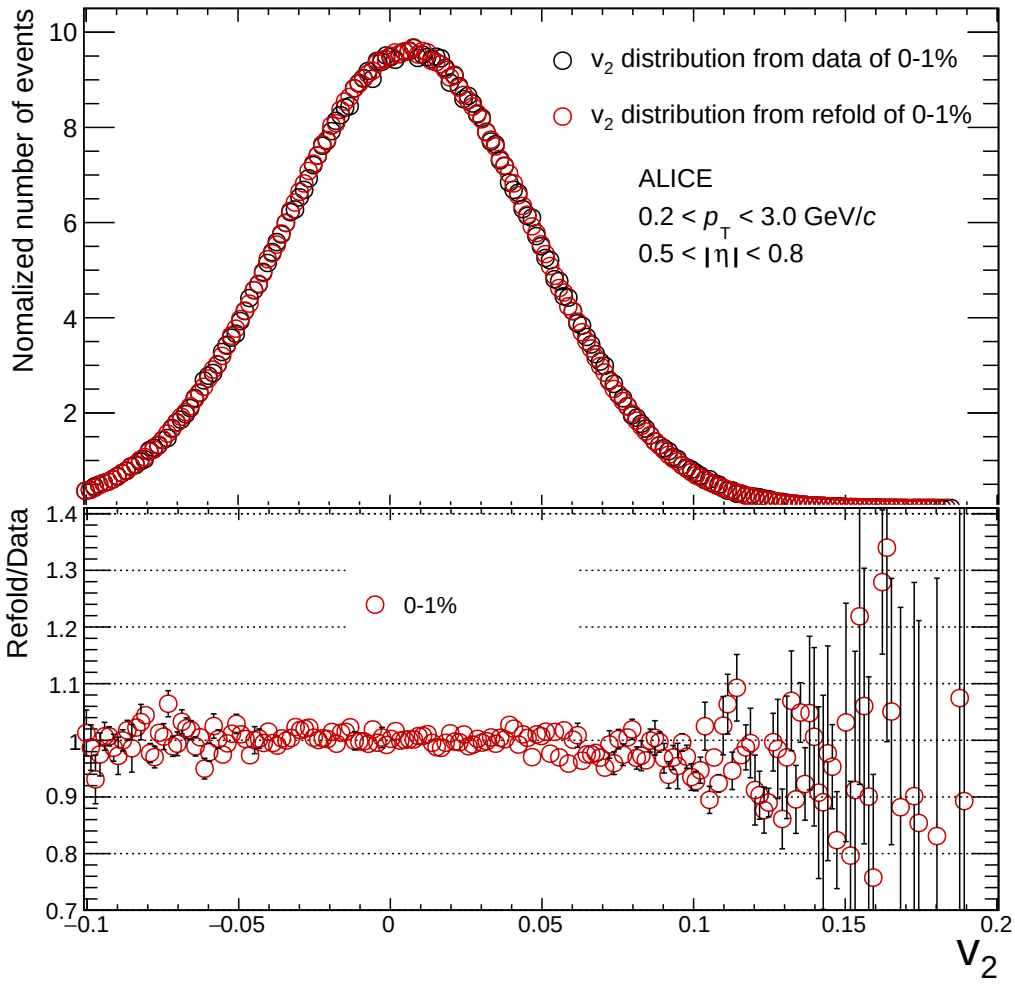

Figure 6.4: Comparison of refolding v_2 and $v_{2\text{obs}}$ cut for 0-1% centrality bin.

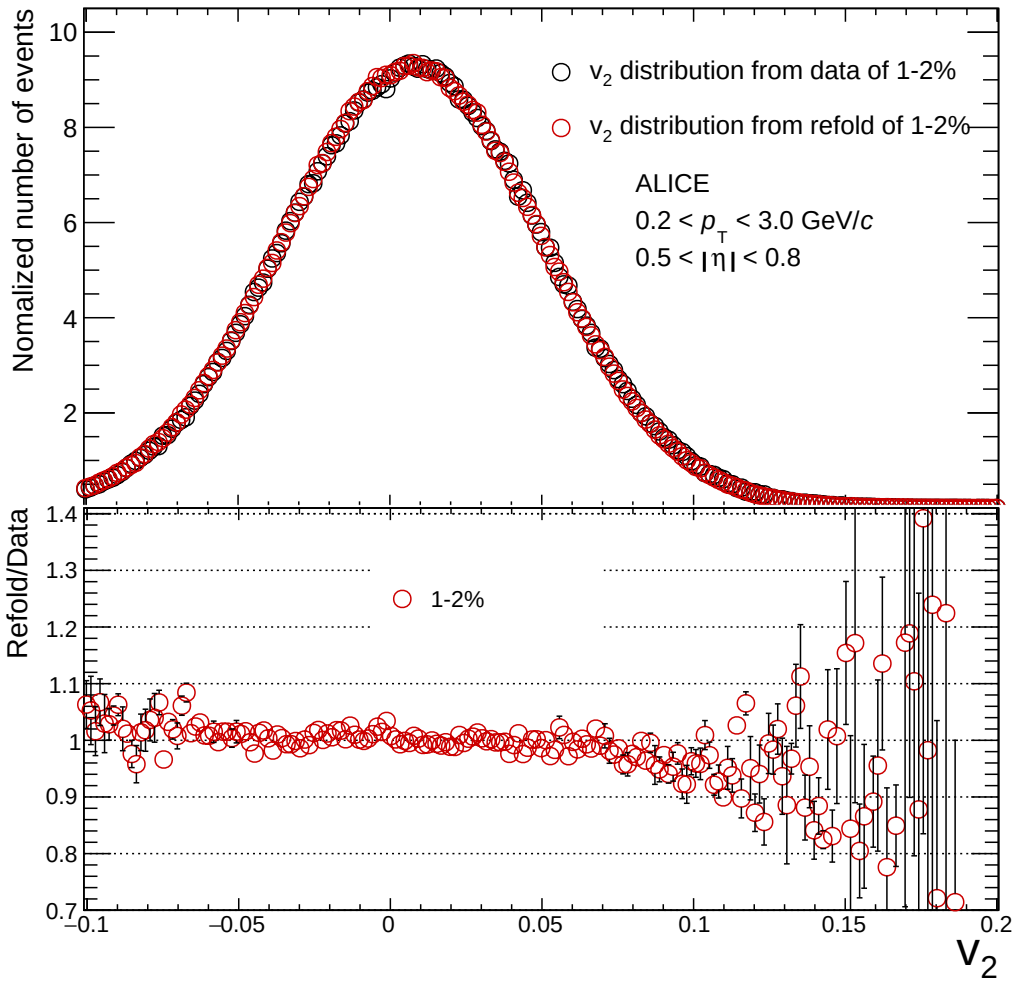

Figure 6.5: Comparison of refolding v_2 and $v_{2\text{obs}}$ cut for 1-2% centrality bin.

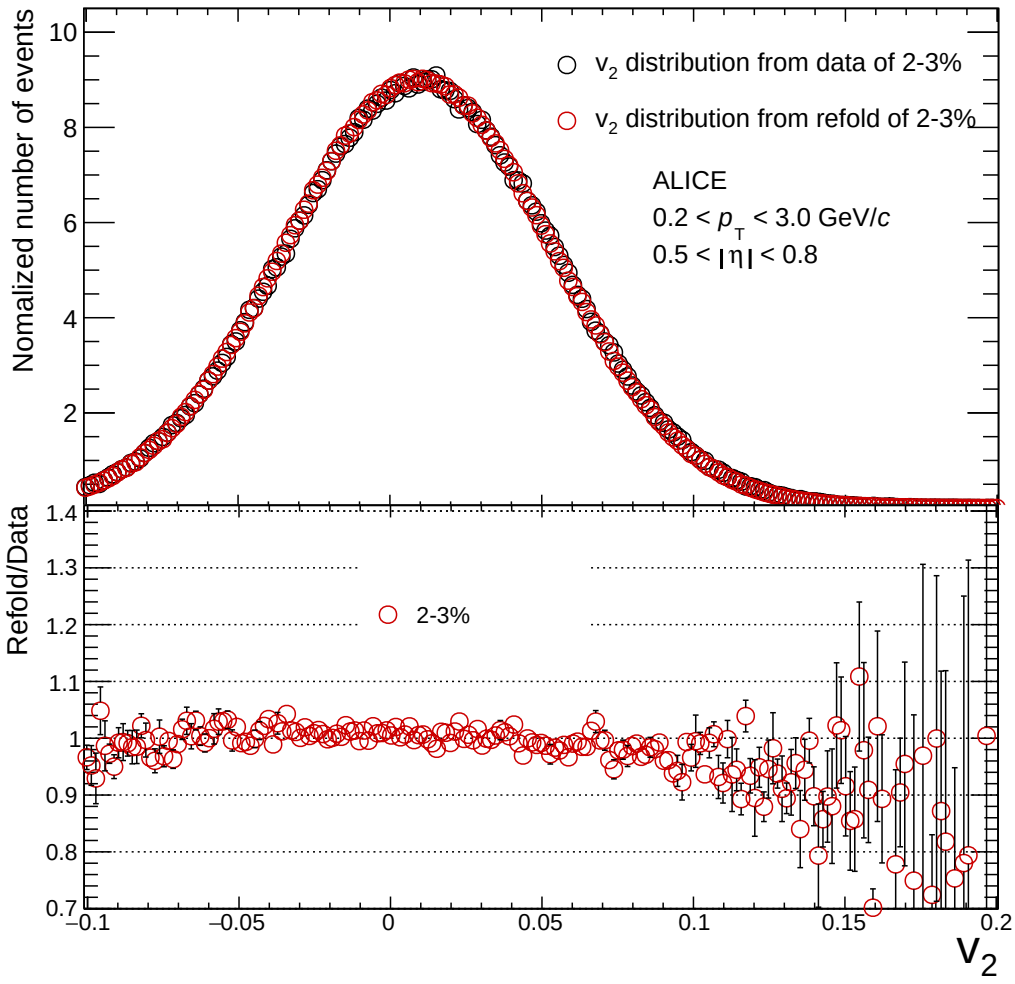

Figure 6.6: Comparison of refolding v_2 and $v_{2\mathrm{obs}}$ cut for 2-3% centrality bin.

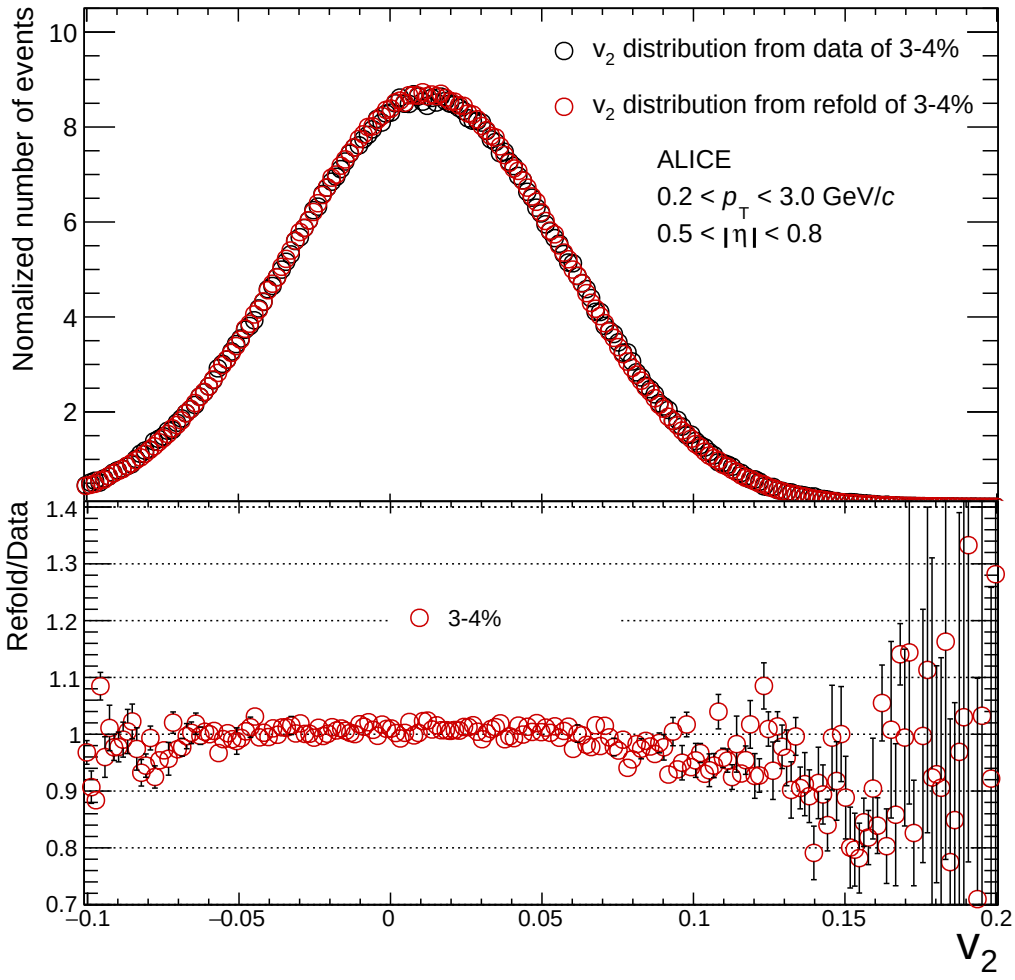

Figure 6.7: Comparison of refolding v_2 and $v_{2\mathrm{obs}}$ cut for 3-4% centrality bin.

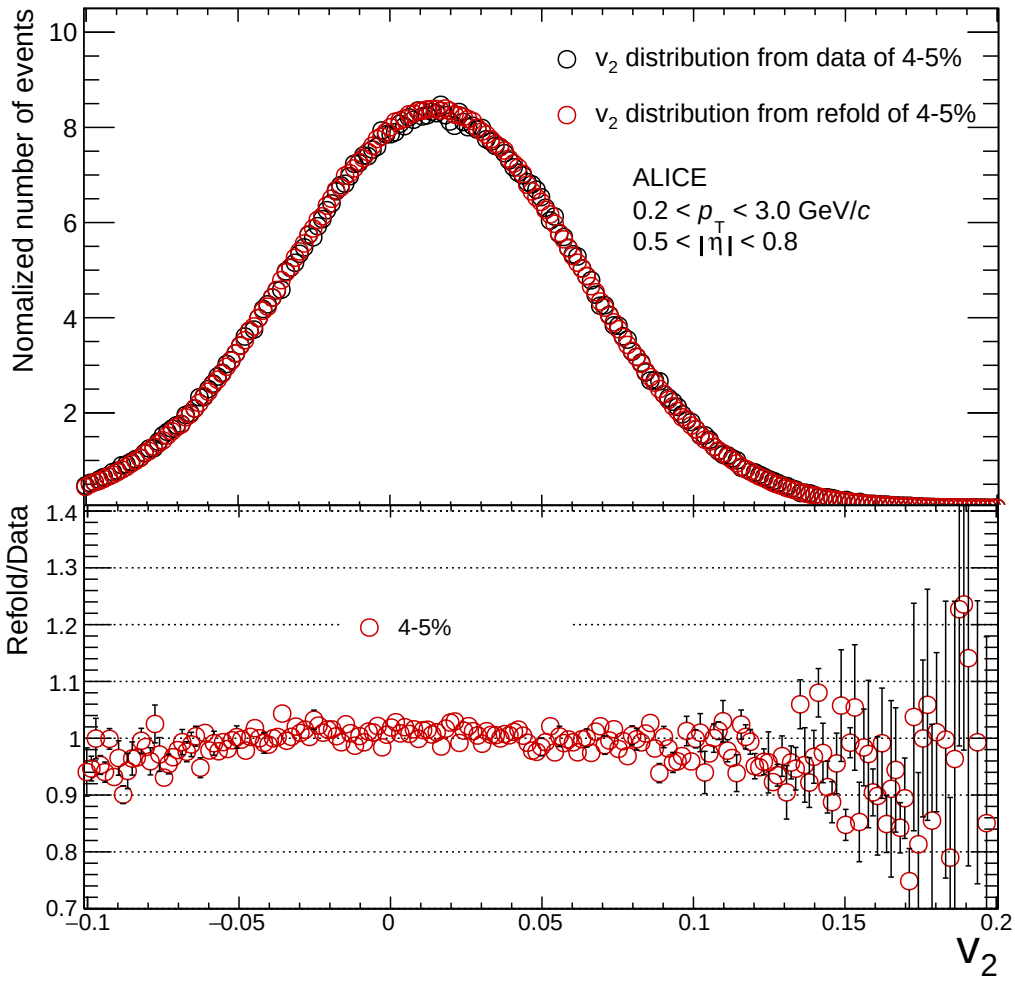

Figure 6.8: Comparison of refolding v_2 and $v_{2\mathrm{obs}}$ cut for 4-5% centrality bin.

6.3 Error Determination

6.3.1 Statistical Error

In order to estimate the statistical errors, a sub sampling technique was used. The v_2 distributions were obtained from five independent sub samples. After such a separation, the standard deviation was obtained to perform a calculation of the statistical errors using the equation below [51]:

$$\sigma = \frac{1}{\sqrt{n}}\sqrt{\frac{\sum(x-\bar{x})^2}{(n-1)}}, \tag{6.7}$$

where σ is the statistical error, and $n = 5$, which is the number of sub samples used.

6.3.2 Systematic Error

In this analysis, three different sources of systematic uncertainty were investigated for the unfolded v_2 distributions. The first one relates to using TPC only tracks data (where only TPC information is used for tracking), rather than the default hybrid tracks (where the both TPC and ITS are used in tracking). As TPC only tracks do not use the ITS, they have a greater contribution from secondary particles which do not originate directly from the heavy ion collision. This turns out to be the largest contribution to the systematic errors. The second source comes from using 8 cm instead of 10 cm as the boundary of the primary vertex cut. With a narrower vertex range, the systematic error due to unsymmetrical multiplicities in the positive and negative η ranges was minimized further. The centrality in the

analysis was determined by the V0 detector as the default, however the TPC was used to determine the centrality. We use the differences of the v_2 dirtribution with respect to the default selections as systematic errors from different sources. These sources were uncorrelated, therefore the final systematic error was calculated with the equation below:

$$\sigma_{sys} = \sqrt{\sigma^2_{\mathrm{TPCTrack}} + \sigma^2_{\mathrm{PVzCut}} + \sigma^2_{\mathrm{TPCCentrality}}}, \tag{6.8}$$

where σ_{sys} is the final systematic error.

Chapter 7

Results

7.1 Full v_2 distributions

As mentioned in Section 4.17, the Elliptic Power distribution is a promising description of eccentricity fluctuations. Combined with Equation 6.3, we obtained the Elliptic Power v_2 distribution as follows:

$$P(v_2) = \frac{2\alpha v_2}{\pi\kappa_2^2}(1-\varepsilon_0^2)^{\alpha+\frac{1}{2}} \int_0^{\pi} \frac{(1-\frac{v_2^2}{\kappa_2^2})^{\alpha-1} d\varphi}{(1-\frac{\varepsilon_0 v_2 cos\varphi}{\kappa_2})^{2\alpha+1}}, \tag{7.1}$$

where α is related to the number of sources that contribute to the eccentricity, v_2 is the underlying second order flow harmonics, and ε_0 is the eccentricity in the reaction plane coordinate system. Equation 7.1 was used to fit the unfolded v_2 distributions. We used χ^2/NDF(number of degrees of freedom) to describe the fitting quality. The results are shown in Figures 7.1 - 7.5.

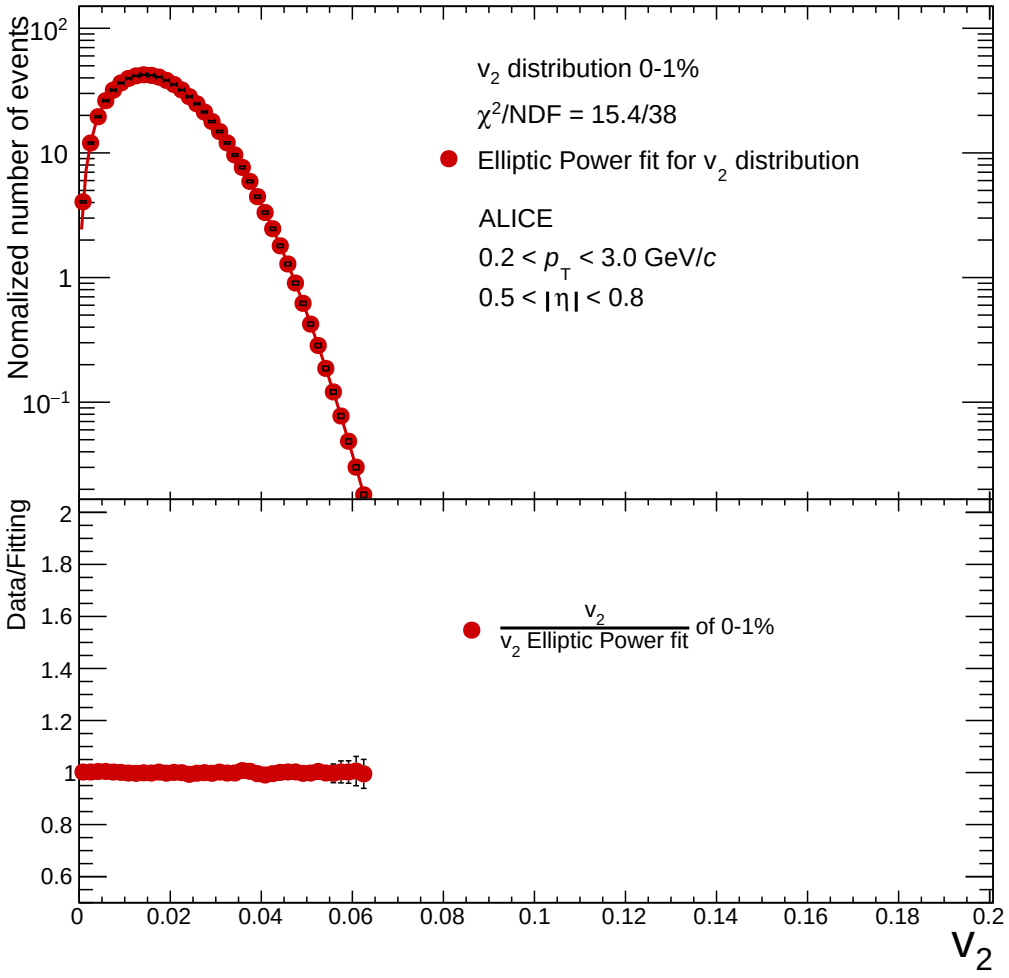

Figure 7.1: Underlying v_2 distribution in 0-1% centrality bin with Elliptic Power fit. Boxes are systematic errors and lines are statistical errors.

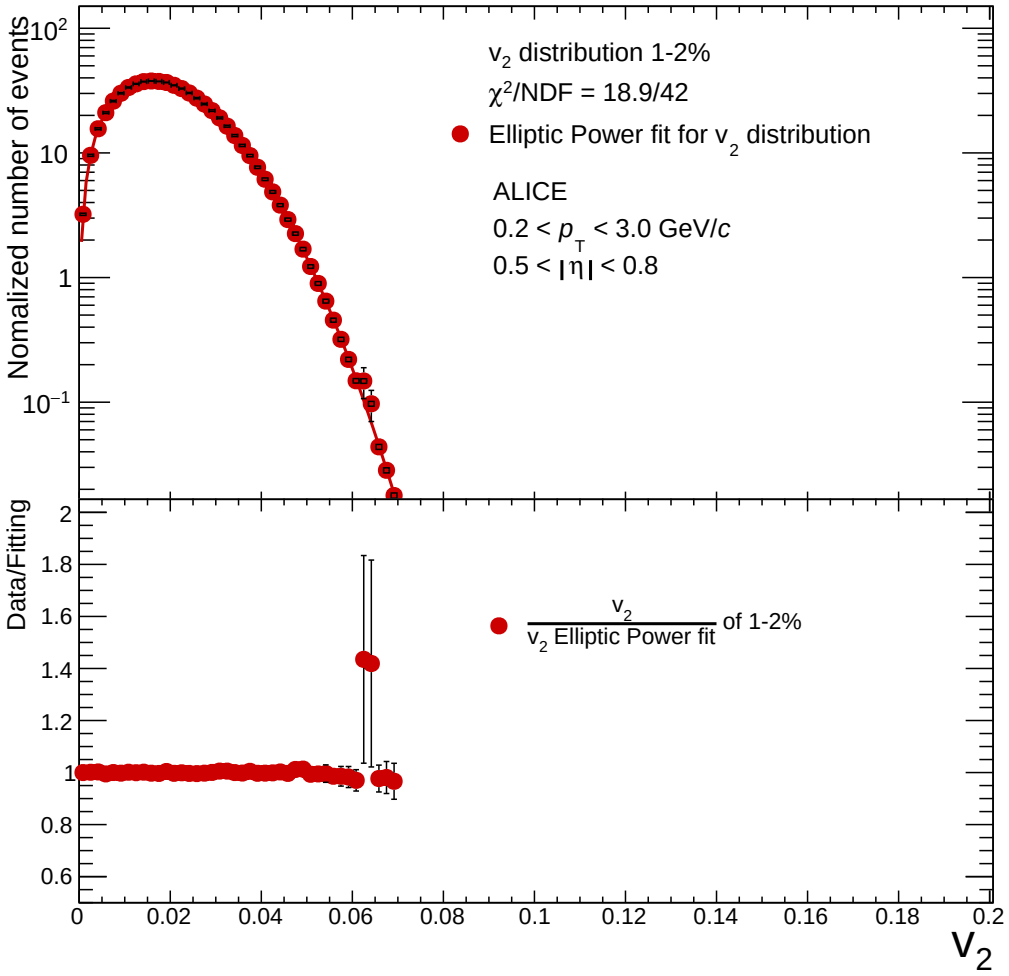

Figure 7.2: Underlying v_2 distribution in 1-2% centrality bin with Elliptic Power fit. Boxes are systematic errors and lines are statistical errors.

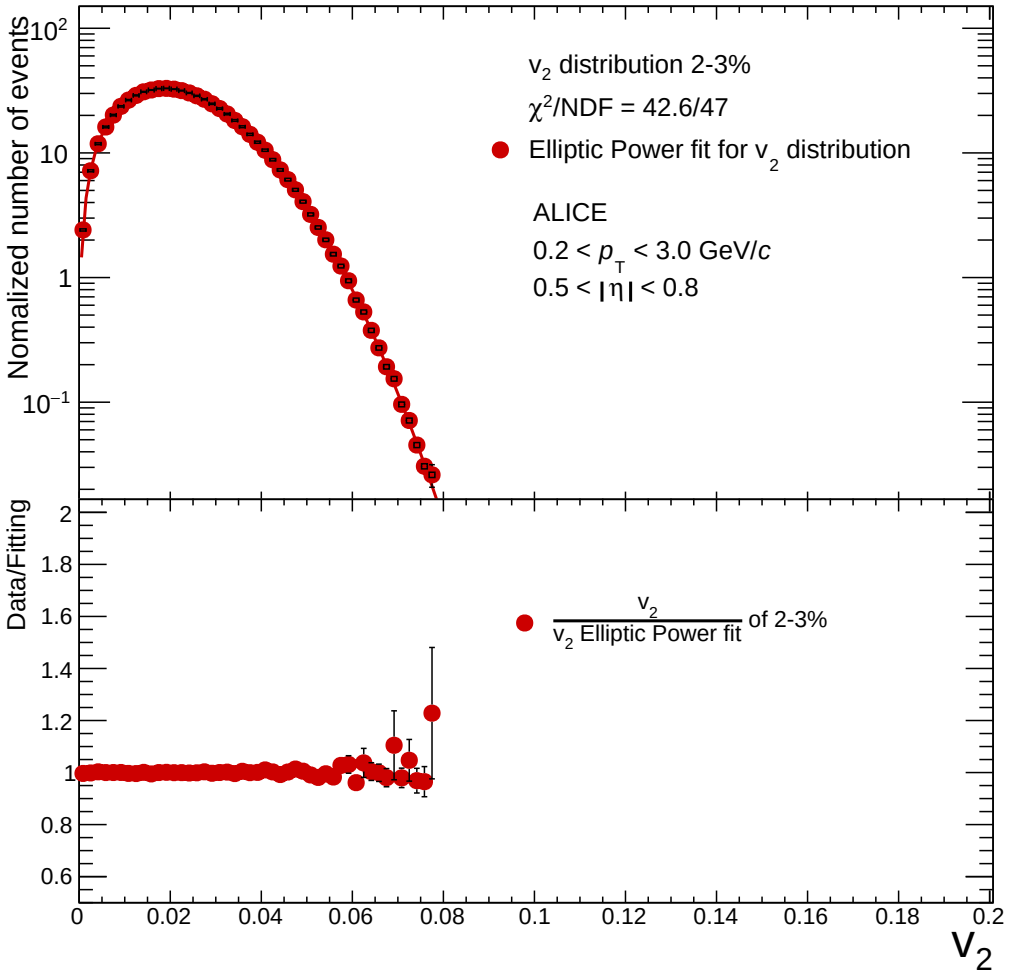

Figure 7.3: Underlying v_2 distribution in 2-3% centrality bin with Elliptic Power fit. Boxes are systematic errors and lines are statistical errors.

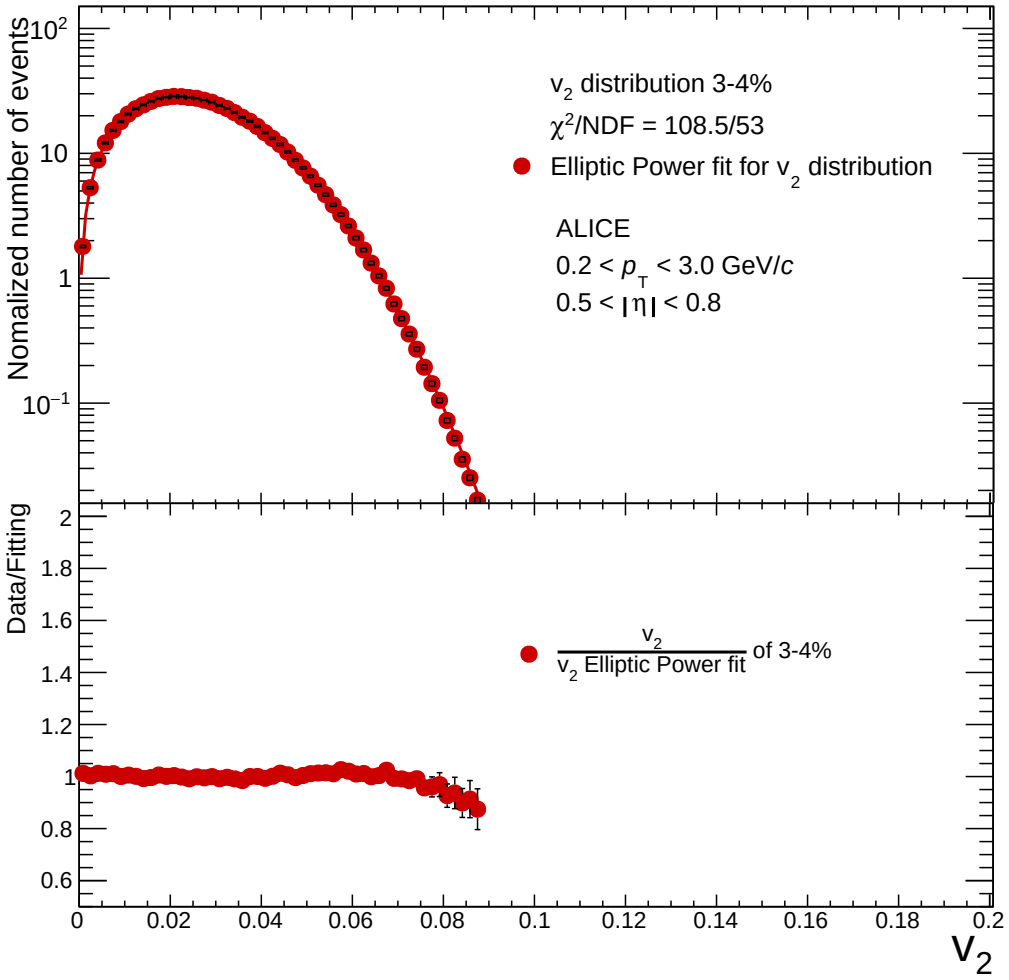

Figure 7.4: Underlying v_2 distribution in 3-4% centrality bin with Elliptic Power fit. Boxes are systematic errors and lines are statistical errors.

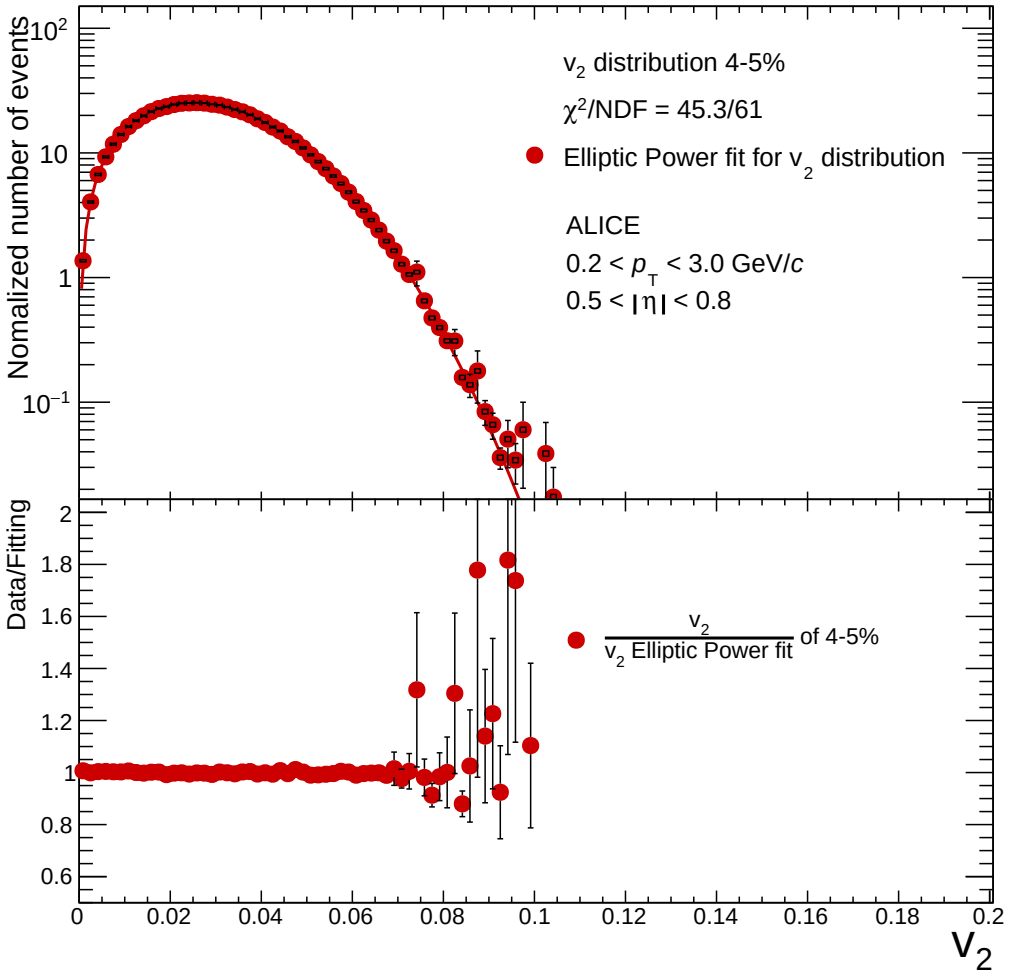

Figure 7.5: Underlying v_2 distribution in 4-5% centrality bin with Elliptic Power fit. Boxes are systematic errors and lines are statistical errors.

The Elliptic Power v_2 distributions described the data well. Only for 3-4% centrality bin, the χ^2/NDF was larger than 1. The fluctuations in the tails was due to low statistics. Table 7.1 shows the comparison of $\langle v_2^2 \rangle$ obtained directly from data

and $\langle v_2^2 \rangle$ from the unfolded results. They are consistent.

Table 7.1: Comparison of $\langle v_2^2 \rangle$ for 0-5% centrality bins

Centrality Bin	0-1%	1-2%	2-3%	3-4%	4-5%
$\langle v_2^2 \rangle_{\text{data}}$	0.000412	0.000533	0.000697	0.000902	0.00113
$\langle v_2^2 \rangle_{\text{unfold}}$	0.000405	0.000513	0.000677	0.000900	0.00115

7.2 α and ε_0

Once the underlying v_2 distribution was obtained from unfolding, we used the Elliptic Power v_2 distribution as discussed in Section 7.1 to fit the distribution and extract two key parameters describing the initial state(IS) of the collision: α and ε_0. This information was used to constrain the initial state models. The comparisons of the two parameters extracted from the unfolded distributions, and the two parameters extracted from T$_{\text{R}}$ENTo model, are shown in Figure 7.6 and 7.7:

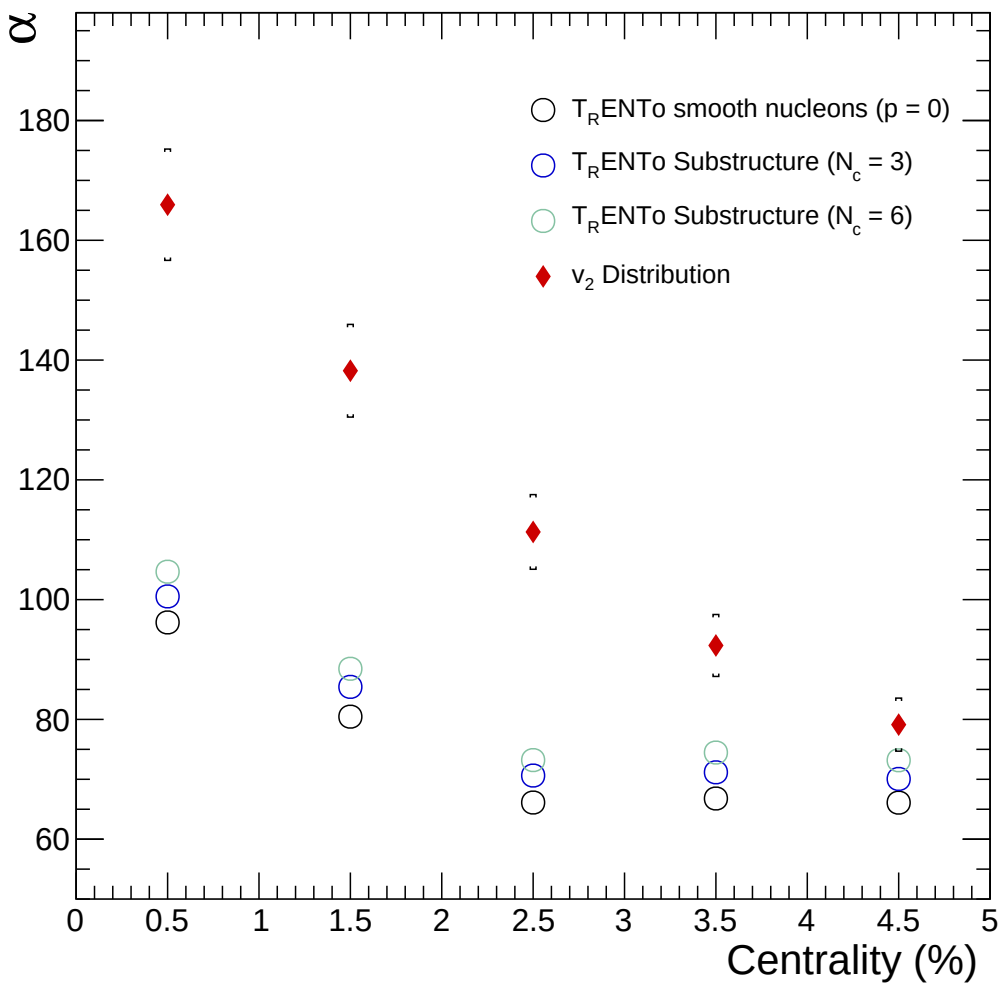

Figure 7.6: Comparison of α between unfolding and different T_RENTo models. Boxes are systematic errors and lines are statistical errors.

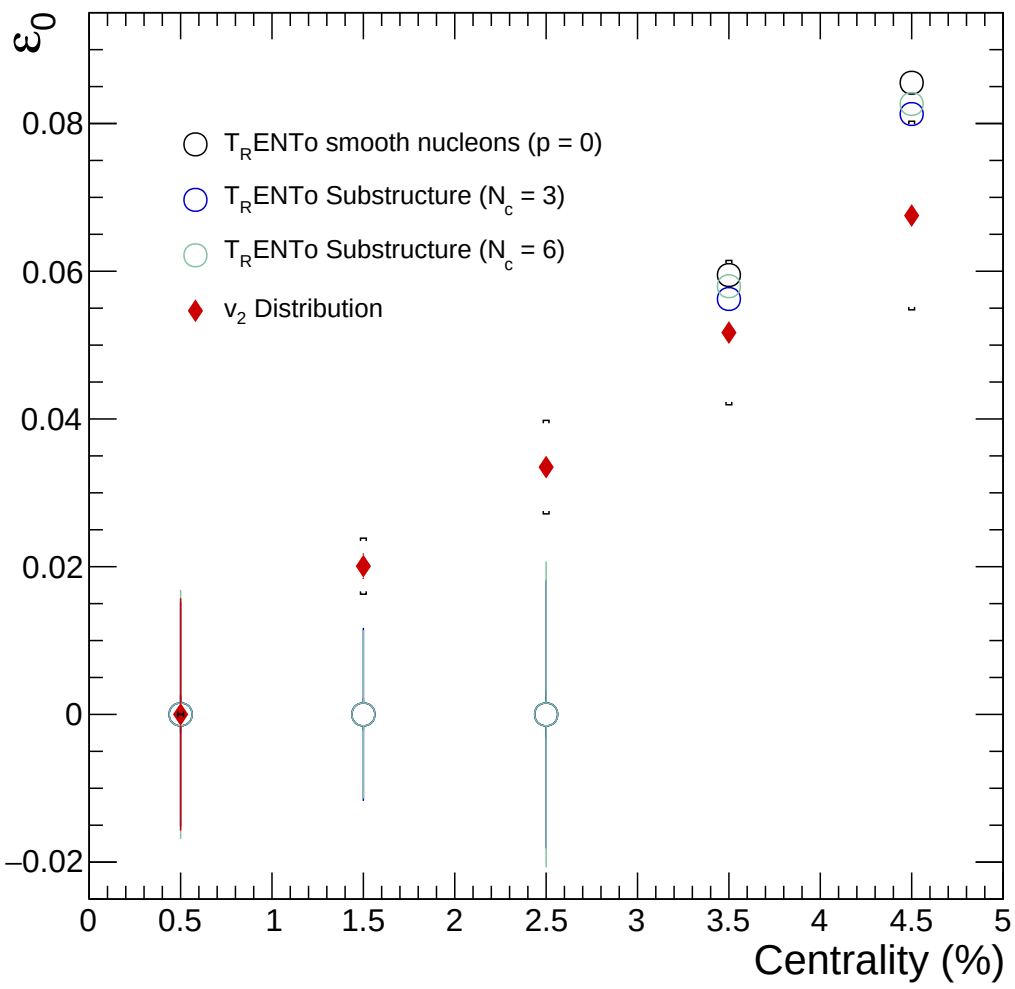

Figure 7.7: Comparison of ε_0 between unfolding and different T$_{\mathrm{R}}$ENTo models. Boxes are systematic errors and lines are statistical errors.

The T$_{\mathrm{R}}$ENTo model is a widely used initial state model [19], and has been used to describe other measurements related to the initial state quite well. A key parameter of the model is the p, which controls the distribution of nuclear matter in the initial

conditions. The parameters N_c corresponds to the number of constituents quarks per nucleon in initial state model.

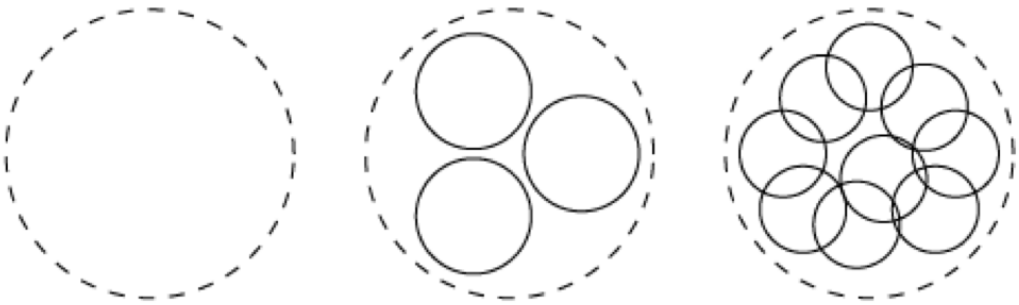

Figure 7.8: Schematic of possible nucleon shapes for $N_c = 1$, $N_c = 3$, $N_c = 9$ [19].

Figure 7.8 illustrates different values of N_c per nucleon. A recent study with the T$_{\mathrm{R}}$ENTo model indicates $N_c = 6$ describes other experimental data from p-Pb and Pb-Pb collisions. In Figure 7.6, values of α from the data are larger than the T$_{\mathrm{R}}$ENTo model predictions, where $\alpha = (N-1)/2$ and N is number of sources that contribute to the eccentricity. The variable ε_0 corresponds to eccentricity in the reaction plane and expected to approach 0 in very central collisions. Figure 7.7 also shows some differences with the data. It can therefore be concluded that the data in this dissertation provides important constraints for such initial-state models.

Chapter 8

Conclusions

The investigation presented in this dissertation has focused on the study of elliptic flow fluctuations in very central collisions for the 0-5% centrality range. The elliptic flow results were obtained from Pb-Pb collisions at the LHC energies of $\sqrt{s_{\rm NN}} = 2.76$ TeV from the LHC running period 1. Understanding elliptic flow fluctuations in the very central region has been a challenge for both experimentalists and theorists. This dissertation aimed to contribute and make steps forward into solving some of the unknown problems in this direction. This dissertation used charged particles measured by the ALICE detector for the kinematic ranges in pseudo-rapidity of $|\eta| < 0.8$, and in the transverse momentum range of 0.2 GeV/c $< p_T <$ 3 GeV/c. Non-flow effects played an important role when investigating elliptic flow. To effectively suppress non-flow effects and minimize statistical uncertainties, we have chosen a $|\eta|$-gap of 1.0.

The elliptic flow observed in Pb-Pb for very central collisions (0-5% centrality)

shows that intrinsic fluctuations in the shape of the nucleus contribute significantly, as the elliptic flow measurements would be expected to be zero if the nuclei were perfectly spherical. This intrinsic fluctuation of v_2 is obtained by unfolding as shown in Chapter 6, and the Elliptic Power distribution described unfolded v_2 distribution well. A unique way to introduce non-flow into the response matrix, which effectively subtracts it, is also provided in this analysis. Furthermore, considering the linear relation between the eccentricity in the initial state and flow harmonics from the final state, theses results provide a unique way to test models of the initial conditions with direct comparisons to experimental data as shown in Figure 7.6 and Figure 7.7. Some differences are observed in the initial state parameters between the data and the widely used $\mathrm{T_R}$ENTo model.

Bibliography

[1] https://atlas.cern/discover/physics.

[2] https://www.bnl.gov.

[3] A. Mocsy and P. Sorensen, "The Sound of the Little Bangs," arXiv:1008.3381 [hep-ph].

[4] http://alice-collaboration.web.cern.ch.

[5] **ALICE** Collaboration, K. Aamodt *et al.*, "Elliptic flow of charged particles in Pb-Pb collisions at 2.76 TeV," *Phys. Rev. Lett.* **105** (2010) 252302, arXiv:1011.3914 [nucl-ex].

[6] J. S. Moreland, J. E. Bernhard, and S. A. Bass, "Alternative ansatz to wounded nucleon and binary collision scaling in high-energy nuclear collisions," *Phys. Rev.* **C92** no. 1, (2015) 011901, arXiv:1412.4708 [nucl-th].

[7] http://home.cern.

[8] **ALICE** Collaboration, B. B. Abelev *et al.*, "Performance of the alice experiment at the cern lhc," *Int. J. Mod. Phys.* **A29** (2014) 1430044, arXiv:1402.4476 [nucl-ex].

[9] **ALICE** Collaboration, K. Aamodt *et al.*, "Alignment of the ALICE Inner Tracking System with cosmic-ray tracks," *JINST* **5** (2010) P03003, arXiv:1001.0502 [physics.ins-det].

[10] **ALICE** Collaboration, A. Kalweit, "Particle identification in the ALICE experiment," *J. Phys.* **G38** (2011) 124073, arXiv:1107.1514 [hep-ex].

[11] http://aliceinfo.cern.ch.

[12] S. G. Weber and A. Andronic, "ALICE event display of a Pb-Pb collision at 5.02A TeV,". https://cds.cern.ch/record/2202730. General Photo.

[13] https://twiki.cern.ch.

[14] **ALICE** Collaboration, J. Adam *et al.*, "Anisotropic flow of charged particles in Pb-Pb collisions at $\sqrt{s_{\rm NN}} = 5.02$ TeV," *Phys. Rev. Lett.* **116** no. 13, (2016) 132302, arXiv:1602.01119 [nucl-ex].

[15] **ALICE** Collaboration, B. Abelev, J. Adam, D. Adamova, M. M. Aggarwal, G. A. Rinella, M. Agnello, A. Agostinelli, N. Agrawal, Z. Ahammed, N. Ahmad, *et al.*, "Multiparticle azimuthal correlations in p-Pb and Pb-Pb collisions at the CERN Large Hadron Collider," *Phys. Rev. C* **90** (Nov, 2014) 054901. https://link.aps.org/doi/10.1103/PhysRevC.90.054901.

[16] S. A. Voloshin, A. M. Poskanzer, A. Tang, and G. Wang, "Elliptic flow in the Gaussian model of eccentricity fluctuations," *Phys. Lett.* **B659** (2008) 537–541, arXiv:0708.0800 [nucl-th].

[17] L. Yan, J.-Y. Ollitrault, and A. M. Poskanzer, "Eccentricity distributions in nucleus-nucleus collisions," *Phys. Rev.* **C90** no. 2, (2014) 024903, arXiv:1405.6595 [nucl-th].

[18] G.-Y. Qin, H. Petersen, S. A. Bass, and B. Muller, "Translation of collision geometry fluctuations into momentum anisotropies in relativistic heavy-ion collisions," *Phys. Rev.* **C82** (2010) 064903, arXiv:1009.1847 [nucl-th].

[19] J. S. Moreland, J. E. Bernhard, and S. A. Bass, "Estimating initial state and quark-gluon plasma medium properties using a hybrid model with nucleon substructure calibrated to p-Pb and Pb-Pb collisions at $\sqrt{s_{\rm NN}} = 5.02$ TeV," arXiv:1808.02106 [nucl-th].

[20] **ALICE** Collaboration, J. Park, "Studies for an upgrade of ALICE Inner Tracking System: Pixel chip characterization," *EPJ Web Conf.* **141** (2017) 08003.

[21] K. G. Wilson, "Confinement of quarks," *Phys. Rev. D* **10** (Oct, 1974) 2445–2459. https://link.aps.org/doi/10.1103/PhysRevD.10.2445.

[22] K. Yagi, T. Hatsuda, and Y. Miake, "Quark-gluon plasma: From big bang to little bang," *Camb. Monogr. Part. Phys. Nucl. Phys. Cosmol.* **23** (2005) 1–446.

[23] Z. Fodor and S. D. Katz, "Lattice determination of the critical point of QCD at finite T and mu," *JHEP* **03** (2002) 014, arXiv:hep-lat/0106002 [hep-lat].

[24] **HotQCD** Collaboration, A. Bazavov *et al.*, "Equation of state in (2+1)-flavor QCD," *Phys. Rev.* **D90** (2014) 094503, arXiv:1407.6387 [hep-lat].

[25] S. A. Voloshin, A. M. Poskanzer, and R. Snellings, "Collective phenomena in non-central nuclear collisions," *Landolt-Bornstein* **23** (2010) 293–333, arXiv:0809.2949 [nucl-ex].

[26] S. R. Coleman and S. L. Glashow, "High-energy tests of Lorentz invariance," *Phys. Rev.* **D59** (1999) 116008, arXiv:hep-ph/9812418 [hep-ph].

[27] **UA5** Collaboration, G. J. Alner *et al.*, "Scaling of Pseudorapidity Distributions at c.m. Energies Up to 0.9-TeV," *Z. Phys.* **C33** (1986) 1–6.

[28] M. Kaur, M. I Adamovich, M. M Aggarwal, Y. A Alexandrov, R. Amirikas, N. P Andreeva, Z. V Anzon, R. Arora, F. A Avetyan, S. K Badyal, A. M Bakich, E. S Basova, I. K Bazarov, K. B Bhalla, A. Bhasin, V. S Bhatia, V. G Bogdanov, V. Bradnova, V. I Bubnov, and D. C Zhou, "Produced particle multiplicity dependence on centrality in nucleus - nucleus collisions," *Journal of Physics G: Nuclear and Particle Physics* **22** (01, 1999) 1469.

[29] C. Lefevre, "The CERN accelerator complex,". https://cds.cern.ch/record/1260465.

[30] **ALICE** Collaboration, G. Dellacasa *et al.*, "ALICE: Technical design report of the time projection chamber,".

[31] C. Garabatos, "The Alice TPC," *Nuclear Instruments and Methods in Physics Research Section A: Accelerators, Spectrometers, Detectors and Associated Equipment* **535** no. 1-2, (2004) 197–200.

[32] **ALICE** Collaboration, C. Zampolli, "Particle Identification with the ALICE detector at the LHC," in *Proceedings, PLHC2012: Physics at the LHC 2012 (PLHC2012): Vancouver, BC, Canada, June 4-9, 2012*. 2012. arXiv:1209.5637 [hep-ex].

[33] **ALICE** Collaboration, E. Abbas *et al.*, "Performance of the ALICE VZERO system," *JINST* **8** (2013) P10016, arXiv:1306.3130 [nucl-ex].

[34] **ALICE** Collaboration, P. Cortese *et al.*, "ALICE technical design report on forward detectors: FMD, T0 and V0,".

[35] **ALICE** Collaboration, A. Toia, "Bulk Properties of Pb-Pb collisions at $\sqrt{s_{NN}} = 2.76$ TeV measured by ALICE," *J. Phys.* **G38** (2011) 124007, arXiv:1107.1973 [nucl-ex].

[36] R. Fruhwirth, "Application of Kalman filtering to track and vertex fitting," *Nucl. Instrum. Meth.* **A262** (1987) 444–450.

[37] S. Voloshin and Y. Zhang, "Flow study in relativistic nuclear collisions by Fourier expansion of Azimuthal particle distributions," *Z. Phys.* **C70** (1996) 665–672, arXiv:hep-ph/9407282 [hep-ph].

[38] B. Alver and G. Roland, "Collision geometry fluctuations and triangular flow in heavy-ion collisions," *Phys. Rev.* **C81** (2010) 054905, arXiv:1003.0194 [nucl-th]. [Erratum: Phys. Rev.C82,039903(2010)].

[39] A. Bilandzic, R. Snellings, and S. Voloshin, "Flow analysis with cumulants: Direct calculations," *Phys. Rev.* **C83** (2011) 044913, arXiv:1010.0233 [nucl-ex].

[40] R. Snellings, "Elliptic Flow: A Brief Review," *New J. Phys.* **13** (2011) 055008, arXiv:1102.3010 [nucl-ex].

[41] N. Borghini, P. M. Dinh, and J.-Y. Ollitrault, "A New method for measuring azimuthal distributions in nucleus-nucleus collisions," *Phys. Rev.* **C63** (2001) 054906, arXiv:nucl-th/0007063 [nucl-th].

[42] N. Borghini, P. M. Dinh, and J.-Y. Ollitrault, "Flow analysis from multiparticle azimuthal correlations," *Phys. Rev.* **C64** (2001) 054901, arXiv:nucl-th/0105040 [nucl-th].

[43] F. G. Gardim, F. Grassi, M. Luzum, and J.-Y. Ollitrault, "Mapping the hydrodynamic response to the initial geometry in heavy-ion collisions," *Phys. Rev.* **C85** (2012) 024908, arXiv:1111.6538 [nucl-th].

[44] H. Niemi, G. S. Denicol, H. Holopainen, and P. Huovinen, "Event-by-event distributions of azimuthal asymmetries in ultrarelativistic heavy-ion collisions," *Phys. Rev.* **C87** no. 5, (2013) 054901, arXiv:1212.1008 [nucl-th].

[45] F. G. Gardim, J. Noronha-Hostler, M. Luzum, and F. Grassi, "Effects of viscosity on the mapping of initial to final state in heavy ion collisions," *Phys. Rev.* **C91** no. 3, (2015) 034902, arXiv:1411.2574 [nucl-th].

[46] R. Brun and F. Rademakers, "ROOT: An object oriented data analysis framework," *Nucl. Instrum. Meth.* **A389** (1997) 81–86.

[47] **ALICE** Collaboration, C. W. Fabjan *et al.*, "ALICE: Physics performance report, volume II," *J. Phys.* **G32** (2006) 1295–2040.

[48] **ALICE** Collaboration, B. Abelev *et al.*, "Technical Design Report for the Upgrade of the ALICE Inner Tracking System," *J. Phys.* **G41** (2014) 087002.

[49] T. Adye, "Unfolding algorithms and tests using RooUnfold," in *Proceedings, PHYSTAT 2011 Workshop on Statistical Issues Related to Discovery Claims in Search Experiments and Unfolding, CERN,Geneva, Switzerland 17-20 January 2011*, pp. 313–318, CERN. CERN, Geneva, 2011. arXiv:1105.1160 [physics.data-an].

[50] **ATLAS** Collaboration, J. Jia, "Measurement of the distributions of event-by-event flow harmonics in Pb-Pb Collisions at $\sqrt{s_{NN}} = 2.76$ TeV with the ATLAS detector," *Nucl. Phys.* **A904-905** (2013) 421c–424c, arXiv:1209.4232 [nucl-ex].

[51] D. N. Politis, J. P. Romano, and M. Wolf, *Subsampling*. Springer Science & Business Media, 1999.